

# Error Modeling for Differential GPS

by

Gregory S. Bierman

B.S.E.E., B.S.E.P., South Dakota State University  
(1989)

Submitted to the Department of Aeronautics and Astronautics in partial  
fulfillment of the requirements for the Degree of

Master of Science in Aeronautics and Astronautics

at the

MASSACHUSETTS INSTITUTE OF TECHNOLOGY

May 1995

© Gregory S. Bierman, 1995. All Rights Reserved.

Signature of Author .....  
Department of Aeronautics and Astronautics  
May 1995

Approved by .....  
Richard E. Phillips  
Charles Stark Draper Laboratory, Inc.  
Technical Supervisor

Certified by .....  
Professor Walter M. Hollister  
Department of Aeronautics and Astronautics  
Thesis Supervisor

Accepted by .....  
Professor Harold Y. Wachman  
Chairman, Department Graduate Committee



# **Error Modeling for Differential GPS**

by

Gregory S. Bierman

Submitted to the Department of Aeronautics and Astronautics on  
May 12, 1995, in partial fulfillment of the requirements for the  
Degree of Master of Science in Aeronautics and Astronautics.

## ABSTRACT

Differential GPS (DGPS) positioning is used to accurately locate a GPS receiver based upon the well-known position of a reference site. In utilizing this technique, several errors sources contribute to position inaccuracy. This thesis investigates the error in DGPS operation and attempts to develop a statistical model for the behavior of this error. The model for DGPS error is developed using GPS data collected by Draper Laboratory. The Marquardt method for non-linear curve-fitting is used to find the parameters of a first order Markov process that models the average errors from the collected data. The results show that a first order Markov process can be used to model the DGPS error as a function of baseline distance and time delay. The model's time correlation constant is 3847.1 seconds (1.07 hours) for the mean square error. The distance correlation constant is 122.8 kilometers. The total process variance for the DGPS model is 3.73 meters<sup>2</sup>.

Thesis Supervisor: Professor Walter M. Hollister

Title: Professor, Department of Aeronautics and Astronautics

Technical Supervisor: Richard E. Phillips

Title: Group Leader, C. S. Draper Laboratory, Inc.



## Acknowledgments

I would like to thank all of those that have helped me in this endeavor. Many have provided guidance and insight that have shaped this thesis and made it what it is.

First of all, I owe great thanks to my advisors, Dick Phillips and Professor Walter Hollister. Dick has overseen my progress every step of the way. I was very fortunate to have such a concerned and involved mentor. Professor Hollister also spent many hours reviewing my work and helping me through the major stumbling blocks.

This thesis would not have been possible without the help of Barry Fink. He collected the data, explained it to me, and provided his software for extraction and ionospheric correction subtraction.

Other members of the Draper staff have been very helpful in many ways and deserve recognition including Bill Robertson, Paul Madden, Ken Spratlin, Tony Bogner, Frank Mullen, and Dennis Brown.

A special thanks to Dr. George Schmidt and Dr. Jesse Ryles for making this opportunity possible.

I thank my parents for supporting me in all I do and giving me a background that helps me succeed.

And finally, I thank my wife, Lisa, for motivating me to continue, helping me to take breaks, and adding so much to my life.

This thesis was prepared at the Charles Stark Draper Laboratory, Inc., under NASA Contract # NAS9-18426.

Publication of this thesis does not constitute approval by the Draper Laboratory or the

sponsoring agency of the findings or conclusions contained herein. It is published for the exchange and stimulation of ideas.

I hereby assign my copyright of this thesis to the Charles Stark Draper Laboratory, Inc., Cambridge, Massachusetts.

---

Gregory S. Bierman

Permission is hereby granted by The Charles Stark Draper Laboratory, Inc. to the Massachusetts Institute of Technology to reproduce any or all of this thesis.

# Table of Contents

Chapter	Page
1 Introduction.....	13
1.1 Motivation .....	13
1.2 GPS Description .....	13
1.3 Differential GPS .....	15
1.4 Previous Work .....	16
1.5 Error Budgets and Modeling .....	17
1.6 GPS Data .....	18
1.7 Thesis Objectives .....	19
2 Data Collection and Formats.....	21
2.1 Draper Rooftop Experiments .....	21
2.1.1 Experiment Description .....	21
2.1.2 Data Description .....	22
2.2 East Coast Experiments .....	23
2.2.1 Experiment Description .....	23
2.2.2 Data Description .....	24
2.3 West Coast Experiments .....	24
2.3.1 Experiment Description .....	24
2.3.2 Data Description .....	25
2.4 Data Anomalies .....	25
3 Data Processing.....	35
3.1 Introduction .....	35
3.2 Inputs to the Processing .....	36
3.3 Definition of the Error and Difference in Errors .....	38
3.4 Auto and Cross Correlation .....	38
3.5 Time Delay Error Analysis .....	41
3.6 Relation of Mean Square Differences to Markov Model .....	43
3.7 Marquardt Method .....	44
3.8 Pseudorange Error Processing .....	45
3.9 Multipath .....	47
4 Results.....	53
4.1 Rooftop Experiment Results .....	53
4.1.1 Navigation Solution for 5-Hour Data .....	53
4.1.2 Navigation Solution for 24-Hour Data .....	59
4.1.3 Pseudorange Errors, 5-Hour Data .....	66
4.1.4 Pseudorange Errors, 24-Hour Data .....	68
4.1.5 Residual Errors .....	71
4.2 East and West Coast Experiment Results .....	75
4.3 Combined Model .....	77

4.3.1	Results From All Sets .....	77
4.3.2	Results From High Confidence Sets .....	80
5	Conclusions and Suggestions for Future Work.....	87
5.1	Conclusions .....	87
5.2	Future Work .....	89
<b>Appendix</b>		<b>Page</b>
A	Marquardt Method .....	91
B	Autocorrelation Limits .....	95



## List of Figures

Figure		Page
Figure 1.1	Differential GPS .....	15
Figure 2.1	Raw X, Y, and Z Errors for Zero Baseline .....	26
Figure 2.2	Satellite Break, Zero Baseline Data .....	27
Figure 2.3	Satellite Switch and Data Gap, Zero Baseline Data.....	28
Figure 2.4	Sample West Coast Data.....	29
Figure 2.5	Close-up of West Coast Data .....	30
Figure 2.6	Raw Data Oscillations, East Coast Data .....	31
Figure 2.7	Navigation Solution Jump Without Satellite Switch .....	32
Figure 3.1	Notional Mean Square Error Model for DGPS.....	36
Figure 3.2	Amount of Data vs. Percent Error.....	41
Figure 3.3	Creating Time Delay Errors .....	43
Figure 3.4	Breaks in Pseudorange Errors .....	47
Figure 3.5	Oscillations in Time Delay Errors, Zero Baseline Data.....	48
Figure 3.6	FFT of Time Delay Errors, Zero Baseline Data.....	49
Figure 3.7	Signal Multipath.....	50
Figure 3.8	Sample Multipath Period for Offset of 20 Meters .....	51
Figure 3.9	Sample Multipath Period for Offset of 1.9 Meters .....	52
Figure 4.1	Satellite ID vs. Time .....	53
Figure 4.2	Navigation Solution Errors .....	54
Figure 4.3	One-Sigma Bounds for Time Delay Errors.....	55
Figure 4.4	Average Navigation Solution Error .....	56
Figure 4.5	Markov Process Fit .....	58
Figure 4.6	Residual for Markov Fit.....	58
Figure 4.7	Satellite ID, 24-Hour Data .....	60
Figure 4.8	Navigation Solution Errors, 24-Hour Data .....	61
Figure 4.9	Mean Error by Time of Day .....	62
Figure 4.10	Average Navigation Solution Error, 24-Hour Data .....	62
Figure 4.11	Markov Process Fit, 24-Hour Data .....	63
Figure 4.12	Residual for Markov Fit, 24-Hour Data.....	64
Figure 4.13	Markov Process Fit, Both 5-Hour and 24-Hour Data .....	65
Figure 4.14	Pseudorange Errors .....	66
Figure 4.15	Average Pseudorange Error .....	67
Figure 4.16	Markov Fit for Pseudorange Error.....	67
Figure 4.17	Residual for Markov Fit, Pseudorange Errors .....	68
Figure 4.18	Pseudorange Error, 24-Hour Data.....	69
Figure 4.19	Average Pseudorange Error .....	69
Figure 4.20	Markov Fit for Pseudorange Error .....	70
Figure 4.21	Residual for Markov Fit, Pseudorange Errors .....	70
Figure 4.22	Markov Fit, All Cases .....	71
Figure 4.23	Residual Errors, All Cases .....	72
Figure 4.24	FFT for Residuals.....	73

Figure 4.25	New Model Fit to Data.....	74
Figure 4.26	Residual for New Markov/Sinusoid Fit .....	75
Figure 4.27	East Coast Baseline Results .....	75
Figure 4.28	West Coast Baseline Results .....	76
Figure 4.29	Navigation Solution Errors, All Data Sets .....	77
Figure 4.30	3-D Error Plot, All Data Sets .....	78
Figure 4.31	Zero Time Delay Results, All Data Sets .....	79
Figure 4.32	Time Delay Errors, High Confidence Sets.....	80
Figure 4.33	3-D Error Plot, High Confidence Sets .....	81
Figure 4.34	3-D Error Plot, No Multipath .....	81
Figure 4.35	Zero Time Delay Results, High Confidence Sets .....	82
Figure 4.36	Markov Process Fit, Distance Dimension.....	83
Figure 4.37	Residual for Markov Fit, Distance Dimension .....	84
Figure 4.38	DGPS Error Model.....	85

## List of Tables

<b>Table</b>		<b>Page</b>
Table 1.1	GPS Static Error Budget .....	17
Table 1.2	Differential GPS Error Budget.....	18
Table 2.1	East Coast Receiver Locations and Types .....	23
Table 2.2	East Coast Baselines .....	23
Table 2.3	West Coast Baselines.....	24
Table 3.1	GPS Data File Format .....	36
Table 4.1	Results for Zero Baseline.....	59
Table 4.2	Results for Zero Baseline, 24-Hour Data.....	65
Table 4.3	Multipath Variances for Each Baseline .....	76



# Chapter 1

## Introduction

### 1.1 Motivation

The Global Positioning System (GPS) is used for navigation and associated tasks in a wide variety of applications. One of the primary modes of GPS operation is differential GPS. Differential GPS allows more accurate positioning than stand-alone GPS. Many new applications are possible because of the increased accuracy obtained through differential GPS. For instance, a cruise missile operating with differential GPS can be guided very accurately to its target destination.

The benefits of differential GPS are apparent, but it must be well understood in order to maximize this benefit. There is a need, therefore, to determine the positioning errors that are associated with differential GPS operation for a variety of cases, then the user can make knowledgeable decisions on the implementation of the differential technique.

### 1.2 GPS Description

GPS signals are transmitted from the satellites at two different frequencies, L1 at 1575.42 MHz and L2 at 1227.60 MHz. The L1 frequency is modulated by two pseudorandom noise codes, C/A-code at 1.023 MHz and P-code at 10.23 MHz. The L2 carrier is only modulated by the P-code. Since the wavelength of the P-code is 30 meters compared to 300 meters for the C/A-code, the P-code provides much better accuracy for positioning. The P-code became known as the Y-code when it was encrypted so only authorized users could access it. A P(Y)-code capable receiver must be “keyed” with the proper information to decode the incoming signals and obtain P-code accuracy. [7]

For C/A-code users, the performance is degraded due to a purposeful degradation in the quality of broadcast orbits and satellite clock dithering. This degradation is called selective availability (SA). [24] An advantage of P-code operation is that performance is not affected by selective availability.

Positioning is accomplished by determining the time it takes for the GPS signals from each satellite to reach the receiver. This time provides an estimate of the distance from satellite to receiver, and “triangulating” using the signals from four or more satellites provides the receiver’s position in three dimensions. The transmit and receive times are corrupted by clock errors, so a true range measurement is not possible. Therefore, the distance measurement from the receiver to each satellite is called the pseudorange.

The “triangulation” is not perfect, because the satellites are not located optimally with respect to the receiver. Additional error is contained in the navigation solution due to the position of the satellites. The instantaneous measure of this error is called the Geometric Dilution of Precision (GDOP). It represents the rms error realized in the navigation solution for unit error in the triangulation measurements. GDOP accounts for dilution of precision in three dimensions and time. GDOP can be broken down into the following components: vertical (VDOP), horizontal (HDOP), time (TDOP), position (PDOP). PDOP reflects the dilution of precision in three dimensions. [20] This can be further decomposed into XDOP, YDOP, and ZDOP.

Incoming GPS signals are delayed when they pass through the earth’s atmosphere. The ionosphere is one of the primary causes for this delay. A P-code receiver can track both the L1 and L2 signals. Since these signals are at different frequencies, the ionospheric delays will be different for each. An estimate for the ionospheric delay can be obtained utilizing the difference between the L1 and L2 delays. Thus a P-code receiver

provides a dual-frequency ionospheric correction term that is subtracted from pseudoranges. Since the L1 and L2 delays are obtained from tracking loops on the signals, additional noise enters the navigation solution when the dual-frequency correction is used. [10]

GPS satellites broadcast almanac files that contain the orbit parameters required to predict the satellites' positions. These files are updated every week in order to maintain the accuracy. All GPS data is referred to by week. The system clock is reset to zero every week on midnight Saturday, so the correct date is found by referencing the GPS week in the data files.

### 1.3 Differential GPS

As shown in Figure 1.1, positioning using differential GPS (DGPS) involves the use of two GPS receivers. One receiver is located at a fixed position that is accurately surveyed, while the other is allowed to move around. The goal is to accurately determine the position of the "roaming" receiver.

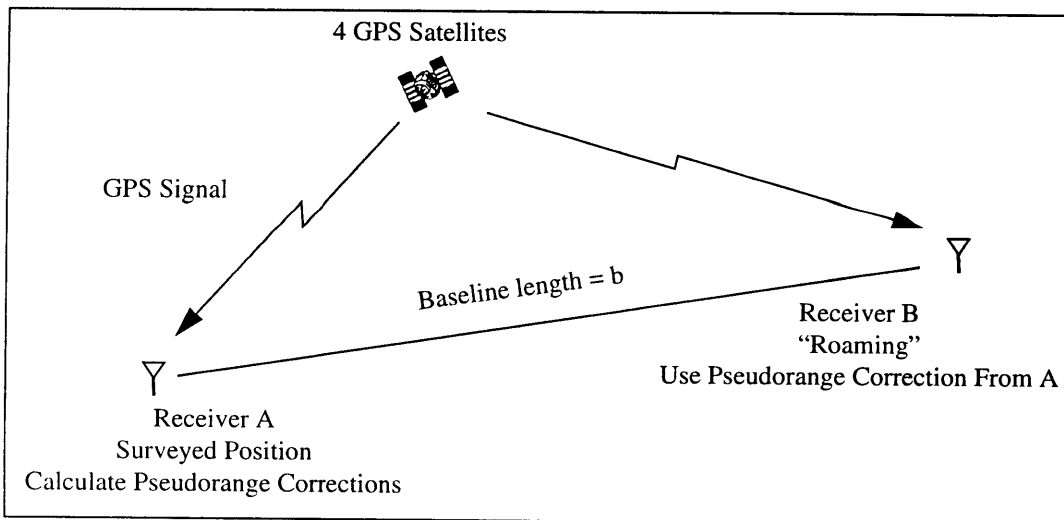


Figure 1.1 Differential GPS

Since the position of receiver A is surveyed, corrections can be determined for the pseudoranges that generate the GPS position. These corrections are then sent to receiver B. The roaming receiver uses the corrections from receiver A to update or correct its position. This procedure is highly accurate with small baseline lengths. Errors increase as the baseline increases or as a time delay is introduced between the measurement and use of the corrections. Such a time delay can be the result of the desire for covert operation.

Using DGPS can help to eliminate errors due to the satellite clock drift, ephemeris errors, and propagation delays. Errors remaining include receiver interchannel biases, receiver noise and quantization errors, multipath, residual propagation delays, and errors due to time delays in the pseudorange corrections. [4]

#### **1.4 Previous Work**

Several sources were found that discussed DGPS errors. Most of the previous work was performed with C/A-code receivers. Error budgets are cited in [4, 15, 17] and depend on the type of receiver being used. For the most part, these budgets were the specifications for the devices or analytic estimates which do not always correlate with actual performance. The next section provides one of these error budgets. An analytic development of the individual error sources was provided in [9].

Two references were found that model GPS and DGPS errors as first order Markov processes. [7, 23] A Markov model was chosen because many physical phenomena exhibit behavior that fit such models reasonably well. No GPS data was used in deriving these models.

One reference used simulated data because receiver data for the desired scenarios was unavailable. [14] Some studies used C/A-code data for their analysis, including



data found on the Internet. [5, 13] One study did use P-code receivers, but this study examined the DGPS errors for a specific geometry and did not develop a model. [25]

This thesis utilizes data segments with common satellites and processes them independently. This prevents jumps in the solutions due to satellite switches from affecting the results. A statistical model for the DGPS errors is provided.

### 1.5 Error Budgets and Modeling

Errors for a P-code receiver are typically cited at about 10 meters RMS in each axis. Table 1.1 shows the error budgets for static GPS operation, and Table 1.2 shows an error budget for Differential GPS. These budgets are specifications for performance for co-altitude receivers at a separation of 50 nmi (92.6 km). They were published by the Air Force GPS Range Applications Joint Program Office. [4, 15]

**Table 1.1: GPS Static Error Budget**

Error Source	C/A-Code Predicted Error (meters)	P-Code Predicted Error (meters)
Satellite Clock Error	3.05	3.05
Ephemeris Error	2.62	2.62
Ionospheric Delay Error	6.40	0.40
Tropospheric Delay Error	.40	0.40
Receiver Noise	2.44	0.24
Receiver Interchannel Bias	0.61	0.15
Multipath	3.05	1.22
UERE (RMS)	8.54	4.25
RMS Horizontal Position Error (HDOP = 1.5)	12.81	6.37
RMS Vertical Position Error (VDOP = 2.5)	21.34	10.62
Total RMS Error	24.89	12.38

**Table 1.2:** Differential GPS Error Budget

Error Source	C/A-Code Predicted Error (meters)	P-Code Predicted Error (meters)
Satellite Clock Error	0	0
Ephemeris Error	0	0
Residual Ionospheric/Tropospheric Delay Error	0.15	0.15
Receiver Noise	2.44	0.24
Receiver Interchannel Bias	0.61	0.15
Multipath	3.05	1.22
UERE (RMS)	3.95	1.26
RMS Horizontal Position Error (HDOP = 1.5)	5.93	1.89
RMS Vertical Position Error (VDOP = 2.5)	9.88	3.15
Total RMS Error	11.53	3.68

The DGPS errors will change as a function of baseline distance and the time delay in the correction inputs. Previous work has estimated the change with baseline distance to be a linear relationship. [13] One of the major challenges in this project will be estimating long term behavior from many segments of short term data.

## 1.6 GPS Data

Several data sets were utilized in this thesis. Draper Laboratory collected all the data. Three data collections were performed: East Coast experiments, West Coast experiments, and zero baseline, rooftop experiments. The first two experiments were performed under a previous effort. They provide GPS data at locations with varying separations so several baselines are available. The experiment names refer to the

region where the experiments were performed, and the objectives for both were the same. The rooftop experiment was performed as part of this thesis. The primary benefit was to be a characterization of the receiver noise. An unexpected benefit was characterization of errors due to multipath. This is possible because the baseline is zero, and both receivers take inputs from the same antenna. These experiments will be described in more detail in Chapter 2. The results from all three experiments will be combined to form a DGPS model from many different cases.

## **1.7 Thesis Objectives**

This thesis will examine the errors in differential GPS as a function of baseline distance between the two receivers and the time delay between when the corrections are computed and when they are used. The final results will include data from P-code receivers only. A model for the errors will be developed and analyzed to determine how well it fits the errors observed in actual differential GPS experiments.

The thesis is organized as follows. Chapter 2 discusses the experiments and the data obtained. Chapter 3 presents methods used in the processing of the data and modeling of the errors. In Chapter 4, the results from each experiment is shown including the performance of the models developed. Chapter 5 is a summary of the thesis and conclusions drawn from the results. Suggestions for future study are also discussed.



## Chapter 2

### Data Collection and Formats

This chapter describes the data that was used to develop the model for DGPS errors. All of this data was collected by Draper Laboratory. Much of it comes from keyed P-code receivers that is unaffected by selective availability.

#### 2.1 Draper Rooftop Experiments

##### 2.1.1 Experiment Description

The goal of the rooftop experiments was to obtain data with a zero baseline and to get an estimate of receiver noise. A GPS antenna was placed on a tripod on the rooftop of Draper. Two Trimble TANS receivers in a laboratory on the 4th floor received the inputs from the single antenna. Since the receivers were getting the exact same inputs, the only difference in their solutions was due to the receivers' internal processing. The baseline is zero meters, and the time delay errors were examined independently of baseline dependent errors. Data was recorded every 10 seconds.

The TANS receivers are keyed P-code receivers which are resistant to selective availability. The position errors are expected to be well within the specified value of 16 meters. A bug in the translation program written for the TANS receivers caused errors in the recorded ephemeris data. A Novatel receiver was positioned on the rooftop to collect data for the same periods as the TANS receivers. The Novatel translation program worked, so it was used as the source of broadcast ephemeris data.

### 2.1.2 Data Description

The first set of data was taken on Monday, November 14th, 1995, 23:44:50 to Tuesday, November 15th, 22:33:10. This was GPS week 775. This set contains approximately 24 hours of data. Unfortunately, one of the computers controlling the TANS receivers failed to store the collected data. All data from one receiver was lost. It was thus not possible to estimate receiver noise from this data. However, the data from the remaining receiver is very useful for the time delay error analysis, because the data can be copied and shifted in time. In many trials comparing receiver A vs. receiver B (two different receivers) with receiver A vs. receiver A (the same receiver), the time shifted errors are statistically identical. Using the same receiver for the time delay study eliminates any sample mean in the data.

The second set of data was taken on Thursday, November 17th, 1995, 17:02:38 to 22:13:40. This was also GPS week 775. This set contains approximately 5 hours of data. This time both computers stored the data, so comparisons between the two receivers could be performed. Unfortunately, a gap of about 1.5 hours occurred in the middle of the data. The gap occurred when neither receiver was able to maintain signal lock on more than three satellites. The reason for the gap has not been determined. Possible explanations include objects blocking the line of sight to the satellite, an inactive GPS satellite, or a satellite that was not correctly transmitting at that time. It is unlikely, however, that any nearby structure could have blocked the satellites for 1.5 hours.

The receivers were configured to track the same four satellites. This was done so the position solution from both receivers would have common error sources. Using solutions from different satellites would mask the differences we are trying to observe.

The receivers were also configured to hold a set of four satellites until the GDOP became greater than 6. At that time, both receivers switched to a new set of four satellites.

## 2.2 East Coast Experiments

### 2.2.1 Experiment Description

The East Coast experiments were conducted in December, 1993. These experiments included both C/A and P-code receivers. Table 2.1 shows the location and type of the receivers used. Data collected from Ft. Stewart, Georgia was not used due to

**Table 2.1 East Coast Receiver Locations and Types**

Receiver Location	Receiver Type
Cambridge, MA	P-code
Portsmouth, NH	P-code
Langley AFB, VA	P-code
Willow Run, MI	C/A-code

problems with the data collection. The East Coast baselines are shown in Table 2.2.

**Table 2.2 East Coast Baselines**

Receiver A Location	Receiver B Location	Baseline Length (km)
Cambridge, MA	Portsmouth, NH	84
Langley AFB, VA	Cambridge, MA	740
Langley AFB, VA	Portsmouth, NH	820
Langley AFB, VA	Willow Run, MI	838
Willow Run, MI	Cambridge, MA	1022
Willow Run, MI	Portsmouth, NH	1052

The C/A-code receiver at Willow Run was a Novatel 951R. The selective availability in the data from this receiver was removed by Aerospace Corporation. The P-code receivers were Trimble 4000SSE unencrypted receivers. The P-code receivers were able to track P-code even though unencrypted, because P(Y)-code encryption was not yet in effect.

### 2.2.2 Data Description

Seventeen different sessions of data were collected. All the receivers were operated at the same time. Some of the sessions were lost due to data collection problems. The data was searched for segments where all receivers had at least twenty-five minutes of time tracking the same four satellites. Five such segments were found in sessions 8, 10, 14, and 16. These five data segments were used to form time delay differences as well as to estimate the differences due to the six baseline separations.

## 2.3 West Coast Experiments

### 2.3.1 Experiment Description

The West Coast experiments were conducted in March, 1994. Keyed P-code Trimble 4000SSE receivers were used at all locations. Only two such receivers were available, however, so each baseline had to be instrumented separately. Data was collected from four baselines as shown in Table 2.3.

**Table 2.3 West Coast Baselines**

Receiver A Location	Receiver B Location	Baseline Length (km)
San Diego, CA	Long Beach, CA	149
Stockton, CA	Fallon, NV	282
Ft. Irwin, CA	Fallon, NV	496
San Diego, CA	Fallon, NV	758



### **2.3.2 Data Description**

Sixteen sessions of data were collected on the west coast, including four sessions per baseline. Data collection problems resulted in the loss of two sessions. For the remaining sessions, data segments of 25 minutes or greater with the two receivers tracking the same four satellites were selected. Each session had from 1 to 5 such segments. These segments were again used to form the time delay differences and to estimate the error due to the four baseline separations.

### **2.4 Data Anomalies**

Several interesting qualities or anomalies have been observed in the collected data sets. These are documented to stimulate future discussion and investigation. The gap in the 5-hour, zero baseline rooftop data has already been mentioned. From discussions with experienced GPS users, satellite outages have occurred on occasion.

The GPS navigation solution jumps at every satellite switch. This is an expected attribute, since it is a function of all four satellites being tracked. One of the primary goals of the data reduction was to deal appropriately with these jumps. Figure 2.1 shows the data from a zero baseline 5-hour rooftop session. The graphs show the components of the difference between one receiver's solution and presumed truth. The vertical lines show the places where the satellite switches occur. Notice the jumps in the

output solution at the satellite breaks. Also note the large data gap in the middle of this set.

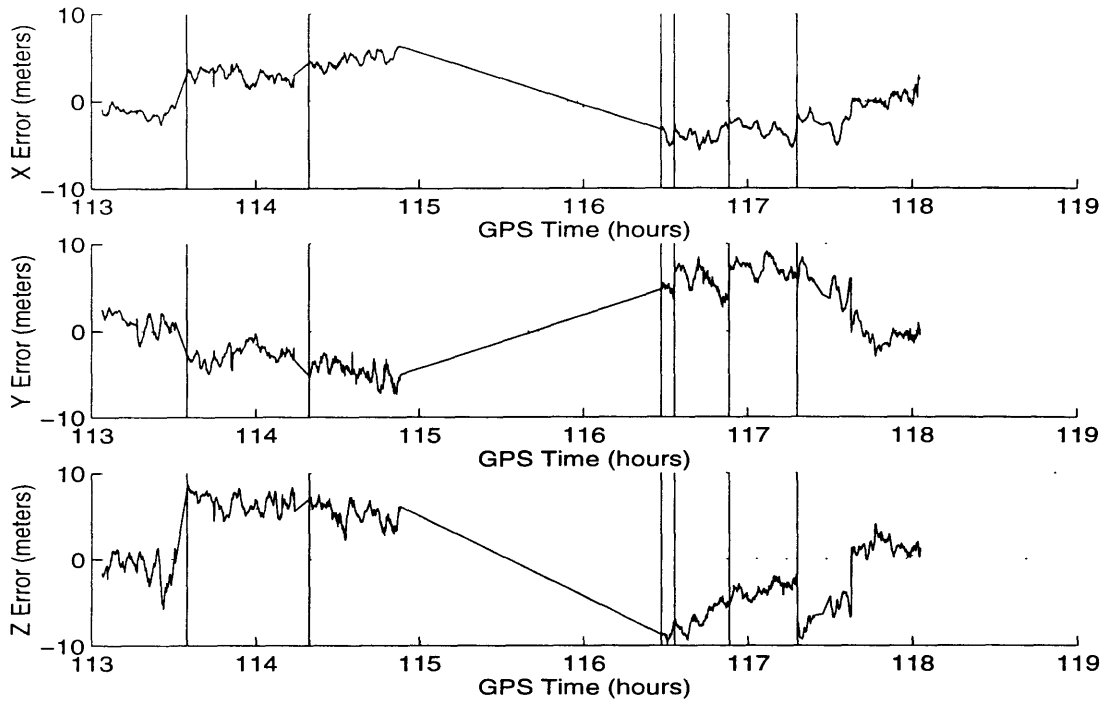


**Figure 2.1 Raw X, Y, and Z Errors for Zero Baseline**

Figure 2.2 shows a close-up of the last satellite break in the zero baseline data. Note the fairly large jumps in both x and z directions.

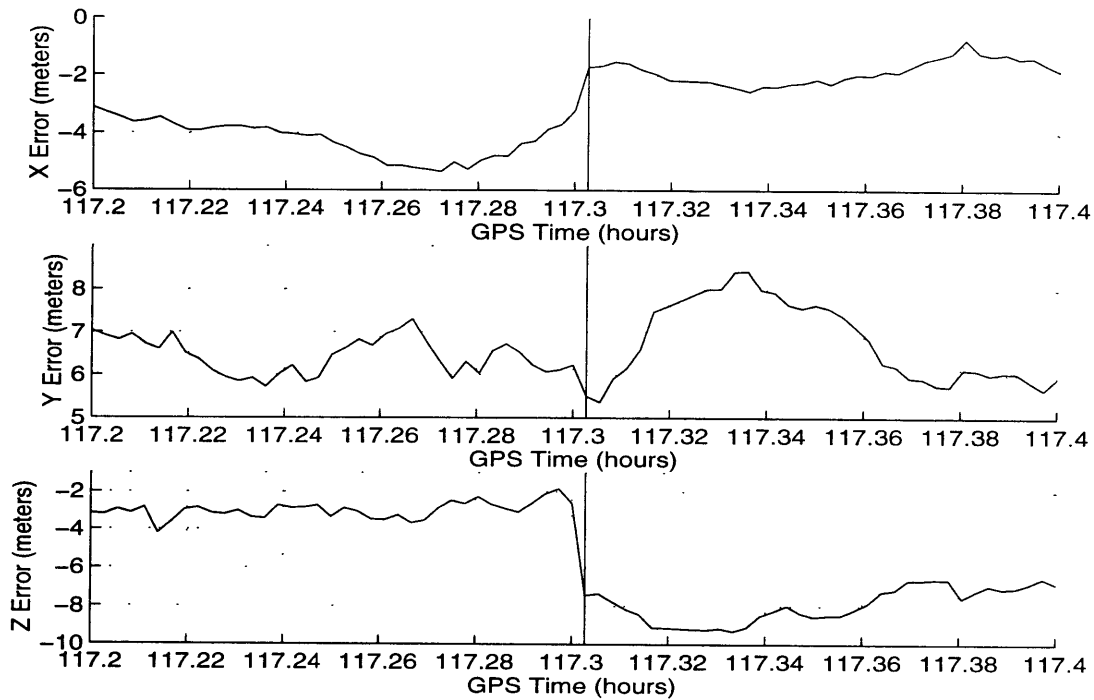


**Figure 2.2 Satellite Break, Zero Baseline Data**

Figure 2.3 shows a close-up of another session of zero baseline data. The vertical lines here are not the satellite switches. They mark each measurement made by the GPS receiver. These occur every 10 seconds. A satellite switch occurred at 114.32 seconds. Note the data gap before the switch. This occurred several times in the collected data, and is presumably due to a delay in locking onto the new satellite.

The errors often exhibited cyclic behavior. A change in the frequency and magnitude of these oscillations is observable at the satellite switches. The oscillations will be primarily attributed to multipath. The changes in the oscillations make sense since the

new satellite set provides a new multipath geometry. This will be discussed further in the next chapter.

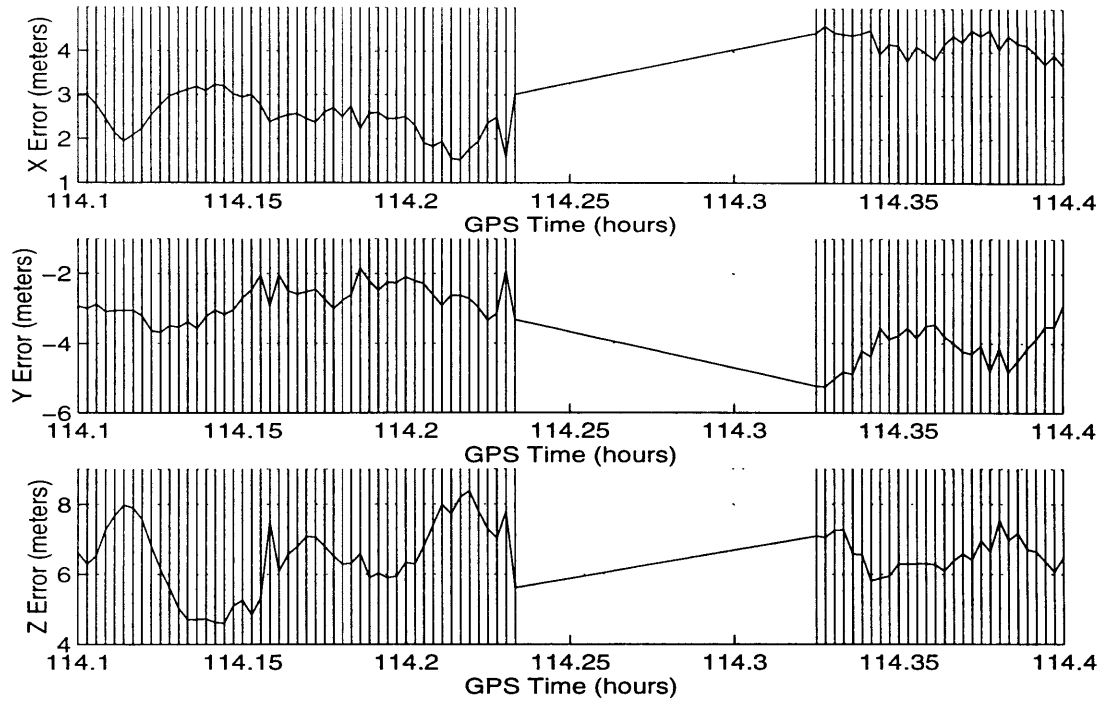


**Figure 2.3 Satellite Switch and Data Gap, Zero Baseline Data**

Figure 2.4 shows a sample of the West Coast data. Again the vertical lines mark each satellite switch. Jumps in one or more components are apparent at each satellite switch.

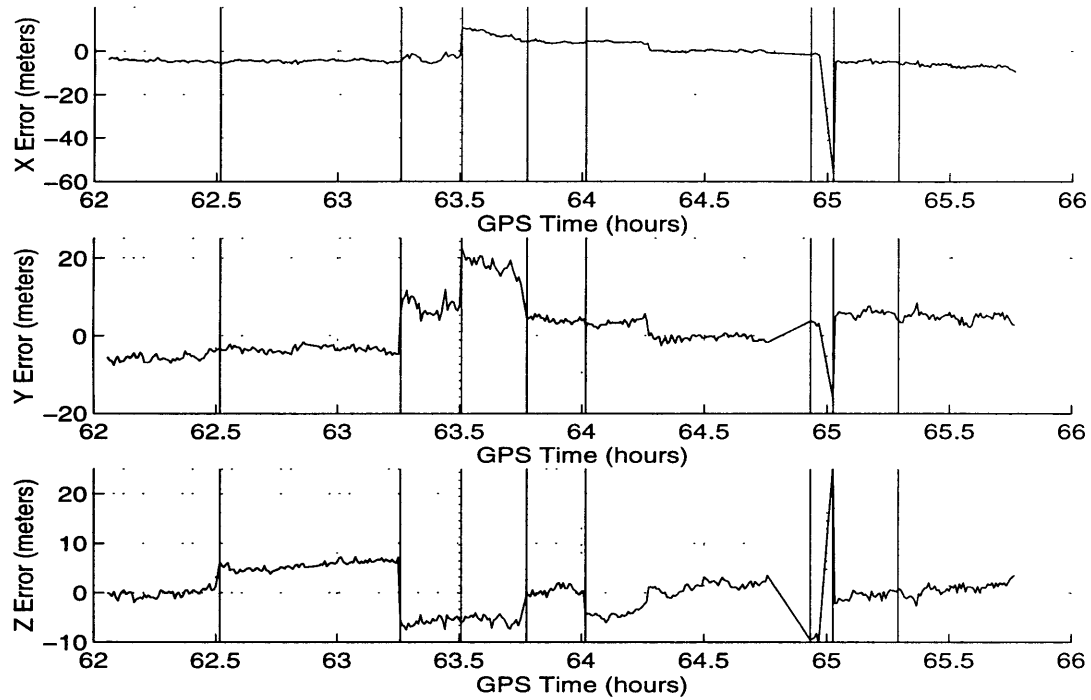


**Figure 2.4 Sample West Coast Data**

Figure 2.5 shows a close-up of the West Coast data. The vertical lines mark each GPS measurement. Data was taken every 30 seconds. A satellite switch occurred at the

jump in the middle of the data set at 63.25 seconds. Note once again the jump in the solution that occurred at the satellite switch.

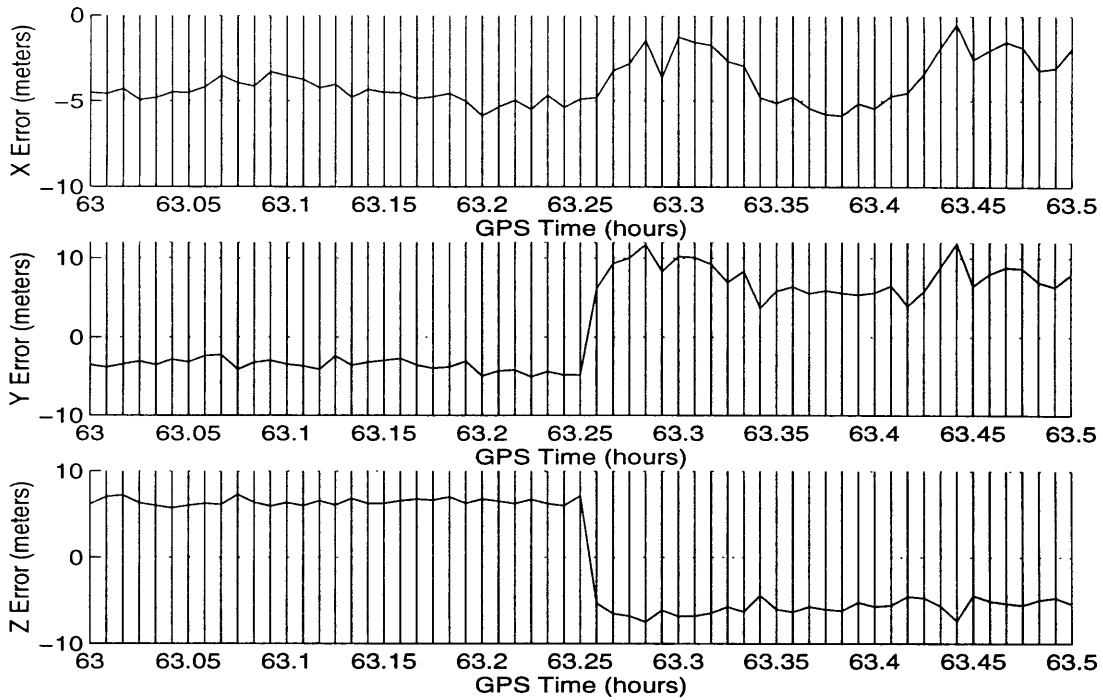


**Figure 2.5 Close-up of West Coast Data**

Figure 2.6 shows an example with only the y direction plotted. Note that satellite switches occurred at 86.8 and 87.1 seconds. The changes in amplitude and frequency of the oscillations in the navigation solution are more observable in this case. Analysis will show that primary oscillation periods change from 71.4 seconds to 90.9 seconds

to 125 seconds for the satellite switches in this example. This was determined by applying a fast Fourier transform to the data.

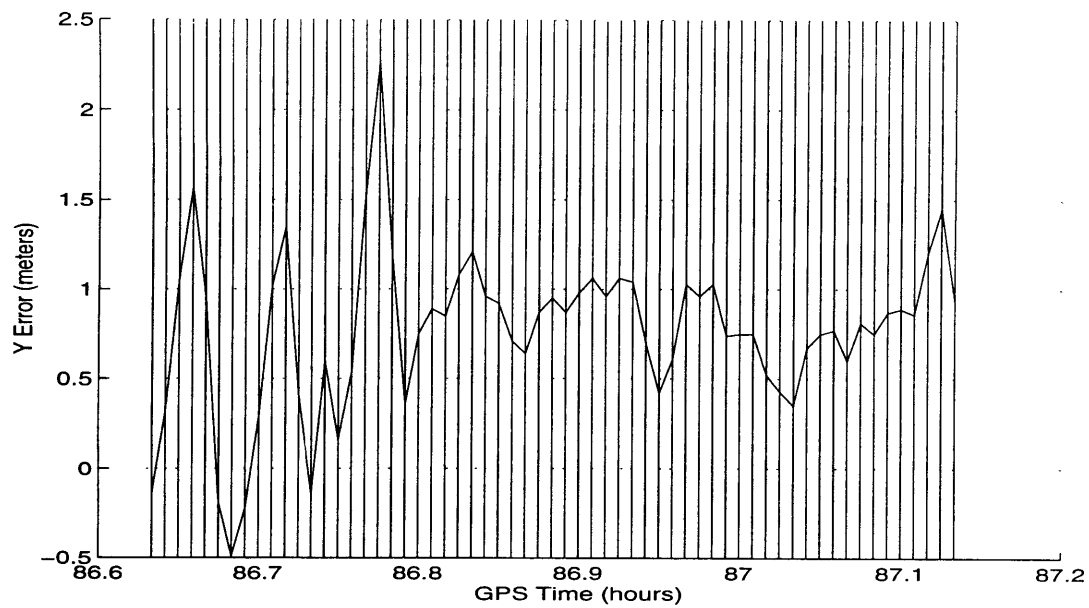


**Figure 2.6 Raw Data Oscillations, East Coast Data**

The GPS navigation solution was observed to jump at points other than satellite switches. In one case, a jump in z position of 7 meters, y of 3 meters, and x of 0.75 meters was observed. Such jumps were rare, and the cause is unknown. One explanation is that the satellite ephemeris was updated at those points. Figure 2.7 shows a

close-up of a jump in the solution when there was no satellite switch. The reader may have noticed this jump in Figure 2.1, towards the very end of the data set.

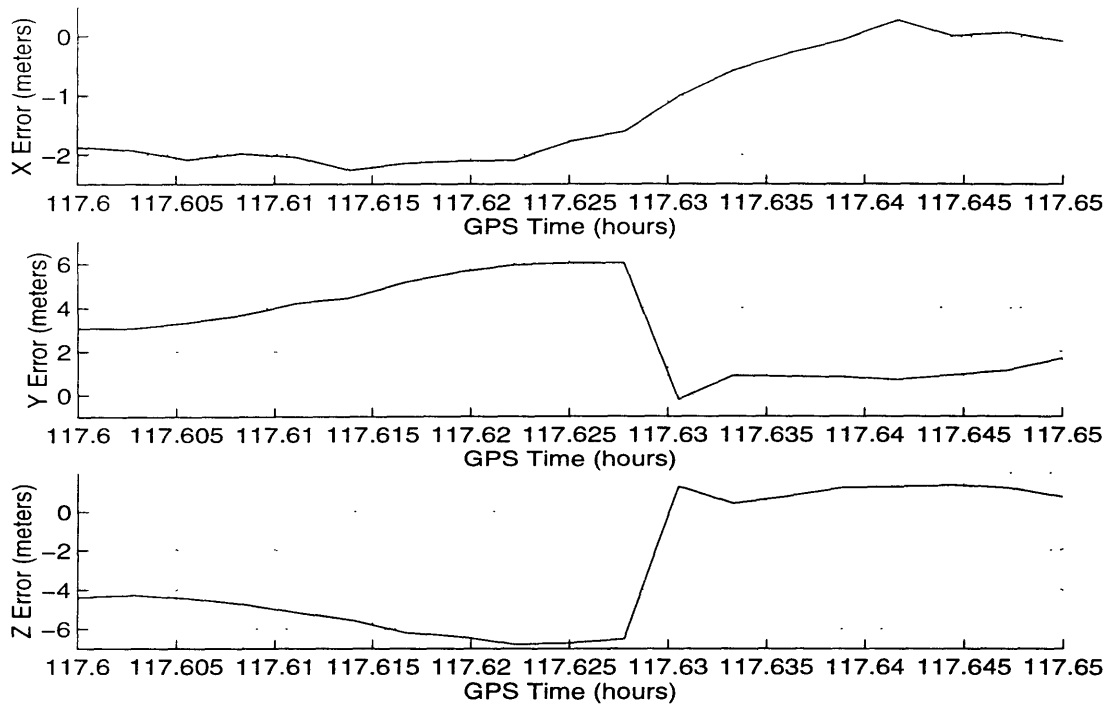


**Figure 2.7 Navigation Solution Jump Without Satellite Switch**

Another anomaly of note was an occasional large and sometimes persistent difference between the position solution from the two receivers. Given that the receivers were being driven by the same antenna, the difference had to have arisen from some internal difference between the two receivers. Sometimes these differences only lasted for one measurement, sometimes they lasted for 100 seconds (10 measurements). A GPS receiver is a complex non-linear device. Such behavior is not surprising and could arise for a number of reasons. Included are low S/N for a particular satellite or some receiver moding change. The level of process noise being introduced into the receiver Kalman filter was such that they were essentially delivering point solutions. This was done, of course, so that no “artificial” time correlation would be introduced into the data. The persistence of the anomalies cannot thus be blamed on the naviga-



tion filter. It should be remembered that the receivers were being forced to hold onto a set of satellites until the GDOP had risen to 7. This would tend to make the solution more sensitive to pseudo-range errors than would normally be the case.

The ephemeris data collected by one of the Trimble receivers was missing some of the satellite information. It appeared to start taking data correctly, but then ephemeris records would show only information from about three of the satellites. Fortunately, the ephemeris from the Novatel receiver was available, so this loss did not affect the results. However, no reason for the data loss has been determined. All other elements of the data from that receiver seemed fine.

The Novatel receiver ephemeris changed GPS week from 775 to 776. This occurred on Thursday, November 17th, at 6:00 p.m. The change in GPS week was expected at midnight on Saturday. The results looked fine and confirmed that the change had actually been made. The almanac data from week 776 was used, and the times from -55 to -49 hours corresponded to 113 to 119 hours of GPS week 775. It is noted that in the Novatel ephemeris file, the almanac entries read week 776, while the navigation solution entries still read week 775.



# Chapter 3

## Data Processing

### 3.1 Introduction

The goal is to observe and model the time and distance correlated behavior of DGPS errors. One such model is a first order Markov process,

$$\text{MSE} = \sigma_{\text{GPS}}^2 \left( 1 - e^{-\frac{t}{\tau} - \frac{x}{x_c}} \right) \quad (3.1)$$

where MSE is the mean square error,  $\sigma_{\text{GPS}}^2$  is the variance of the Markov process,  $\tau$  is the time correlation constant, and  $x_c$  is the distance correlation constant. A notional plot of this model is shown in Figure 3.1. We will focus for the most part on Markov models because of their utility in navigation error analysis. The basic underlying phenomena which cause these errors may introduce correlation between the time and distance behavior. An example would be a traveling ionospheric disturbance. Over an

ensemble of cases, however, the correlation is expected to be zero. It will be so assumed for this study.

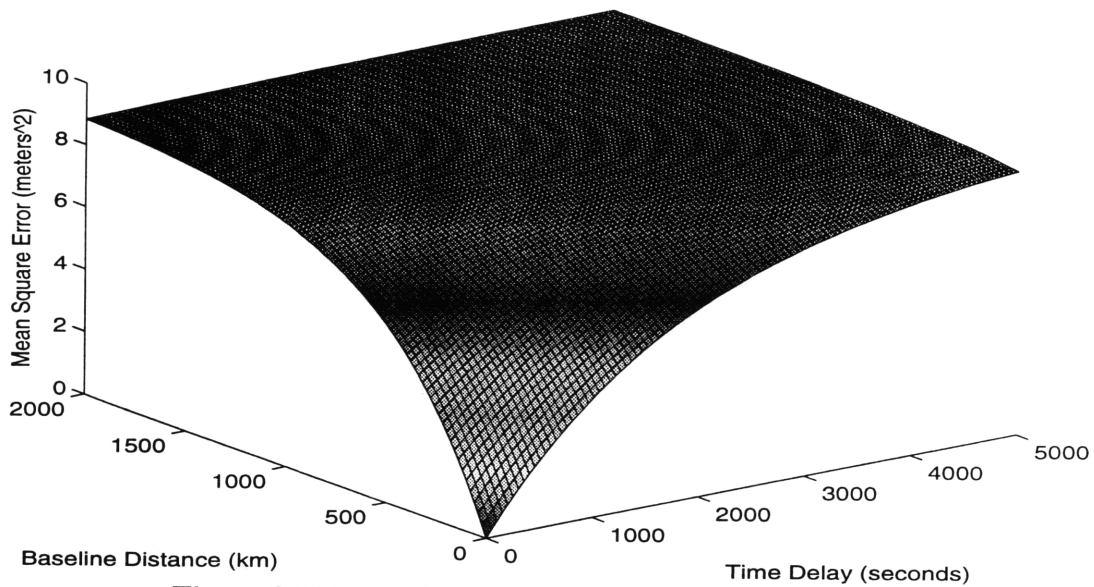


**Figure 3.1 Notional Mean Square Error Model for DGPS**

### 3.2 Inputs to the Processing

The first step in the processing was to remove corrections for ionospheric delay. This eliminates the noise from the  $L_2$  channel, reducing the noise level by a factor of  $\frac{1}{\sqrt{2}}$ . Differencing outputs from the two receivers will cancel the ionospheric errors to the extent that they are the same. This is a common practice in DGPS operation. Further characterization of this residual ionospheric error is one of the goals of the study. Removal of the ionospheric correction was actually done prior to the start of this study. [10] The format for the data is shown in Table 3.1.

**Table 3.1 GPS Data File Format**

1	2	3	4	5	6	7	8	9
Time	X	Y	Z	# Sats	Prn1	Prn2	Prn3	Prn4
10	11	12	13	14	15	16	17	18
Prn5	Prn6	GDOP	PDOP	HDOP	VDOP	TDOP	Status	Clock

The measurements from the two receivers A and B were edited by deleting measurements for which the time tags could not be matched. In addition, measurements were used only when the receivers indicated that the solution was good (status flag = 1).

Satellite switch times were computed in order to split the data into different sets that used the same four satellites for the entire set. This intentionally eliminates satellite switching as one of the sources of decorrelation. A negative aspect of this strategy is that we will be trying to estimate long term behavior from a number of short term data segments. This will be discussed in more detail later. The data segments were samples from what is presumed to be a zero mean process. The small sample size introduced a sample mean into the data. This mean was removed before determining the correlation between different data sets.

Another strategy for getting as close to the underlying phenomenon as possible, i.e. errors in the pseudo-ranges, was to normalize the errors in the position solution components using the dilution of precision in each component, XDOP, YDOP, and ZDOP. These values were computed by utilizing a GPS constellation simulation and inputting the measurement times for each set of data and the satellites tracked by each receiver. [6] The program makes use of the almanac file taken from the Novatel receivers. The DOP values were obtained from the diagonal of the  $(H^T H)^{-1}$  matrix. The resulting DOPs were used to normalize the x, y, and z errors.

For the rooftop, zero baseline data the GPS antenna was not placed at the surveyed marker. (The marker is in the “shadow” of a large vertical metal wall.) The placement was in an attempt to minimize multipath effects on the solution. Therefore, the truth value for the position (x, y, z) was defined to be the average position for all the data sets. This differed from the surveyed position by  $x_{\text{surv}} - 5.6590$  meters,

$y_{\text{surv}} + 5.8299$  meters, and  $z_{\text{surv}} + 18.7744$  meters. These values were in the right direction and distance from the marker - as well as could be determined by eyesight. No effort was made to actually measure the distance, since it was noted that the survey marker position was itself only accurate to about a meter. [21]

### 3.3 Definition of the Error and Difference in Errors

This section defines the errors that were utilized in the autocorrelation processing. The quantity of interest is, finally, the difference in error between the time shifted errors from receiver A and/or B.

$$x_{\text{diff}} = (x_{\text{err}}(t + \Delta t) - x_{\text{err}}(t)) / \text{XDOP} \quad (3.2)$$

The RSS difference is

$$\text{DIFF}_{\text{RSS}} = \sqrt{x_{\text{diff}}^2 + y_{\text{diff}}^2 + z_{\text{diff}}^2} \quad (3.3)$$

The individual components of the error at each receiver are defined by:

$$x_{\text{err}} = x_{\text{msd}} - x_{\text{true}} \quad (3.4)$$

These individual errors are split into six sets where all the points in a set use the exact same four satellites. The RSS for each set was found using Equation (3.3).

### 3.4 Auto and Cross Correlation

The first strategy for characterizing the behavior of the differences was to examine the correlation in the rooftop data. The cross correlation and the autocorrelation of the rooftop, zero baseline, differences was computed. Since the two receivers were being driven from the same antenna, and the receivers were only contributing white noise, the cross and auto correlation were expected to both be measures of the same thing,

the behavior of the errors in pseudorange with time. This analysis was done for the component differences and the RSS difference for each of 6 data sets.

The cross correlation between receiver A and B differences was found. The sample mean was subtracted from the data before the correlation algorithm was applied. Correlations were found for x, y, z, and the RSS differences for each set from 1 to 6 using Equation (3.2) and (3.3).

The sigma and tau values were estimated for each set. The variance,  $\sigma^2$ , is the center value, since the inputs were of zero mean. Tau is the value on the x axis that corresponds to a y value of  $\frac{\sigma^2}{e}$ .

A Markov process has a probability distribution that is dependent only on the value at one point immediately in the past. The process can be described by Equation (3.5), where w is white noise and  $\beta$  is the reciprocal time constant. [12]

$$\frac{dx}{dt} + \beta (t) x = w \quad (3.5)$$

The autocorrelation of a zero mean Markov process is given by Equation (3.6). The correlation time, or 1/e point, is found at  $1/\beta$ . [12]

$$\phi_{xx}(\tau) = \sigma^2 e^{-\beta|\tau|} \quad (3.6)$$

A single variance and time constant for the six set ensemble was found in two ways: a) by finding the correlation of the weighted average of the data in the six sets, and b) taking the weighted average of the variance and time constant found from the correlation of each of the six sets.

The results of the cross-correlation process were disappointing for two reasons. The first is that a tremendous amount of data is required to get accurate results using

this technique. Brown and Hwang [7] present the limit on experimental autocorrelation as

$$\text{Var}[V_x(\tau)] \leq \frac{2\sigma^4}{\beta T} \quad (3.7)$$

where  $\frac{1}{\beta}$  is the time constant,  $V_x(\tau)$  is the experimentally determined autocorrelation function,  $T$  is the time length of the experimental record, and  $\sigma^2$  is the variance of the process.

For a requirement of 10% accuracy on the estimation of the autocorrelation function, the experimental autocorrelation should have a standard deviation less than 0.1 times  $\sigma^2$ , or 0.01 times  $\sigma^4$ . Therefore,  $\frac{\text{Var}[V_x(\tau)]}{\sigma^4} = 0.01$ , and the limit becomes

$$T = \frac{2}{0.01\beta} \quad (3.8)$$

for an accuracy of 10%. If the time constant  $\left(\frac{1}{\beta}\right)$  is 1800 seconds,  $T = 360,000$  seconds. In other words, 4.2 days of data is required. In general, the data required for 10% accuracy equals 200 times the time constant. A time constant of 250 seconds requires almost 14 hours of data for 10% accuracy. The development of the accuracy limit is presented in Appendix B.

Figure 3.2 is a graphic expression of Equation (3.7). It shows the plot of amount of data vs. percent error in the autocorrelation function for a process with a time constant



of 1800 seconds. Again, note that about four days worth of data is required in order to

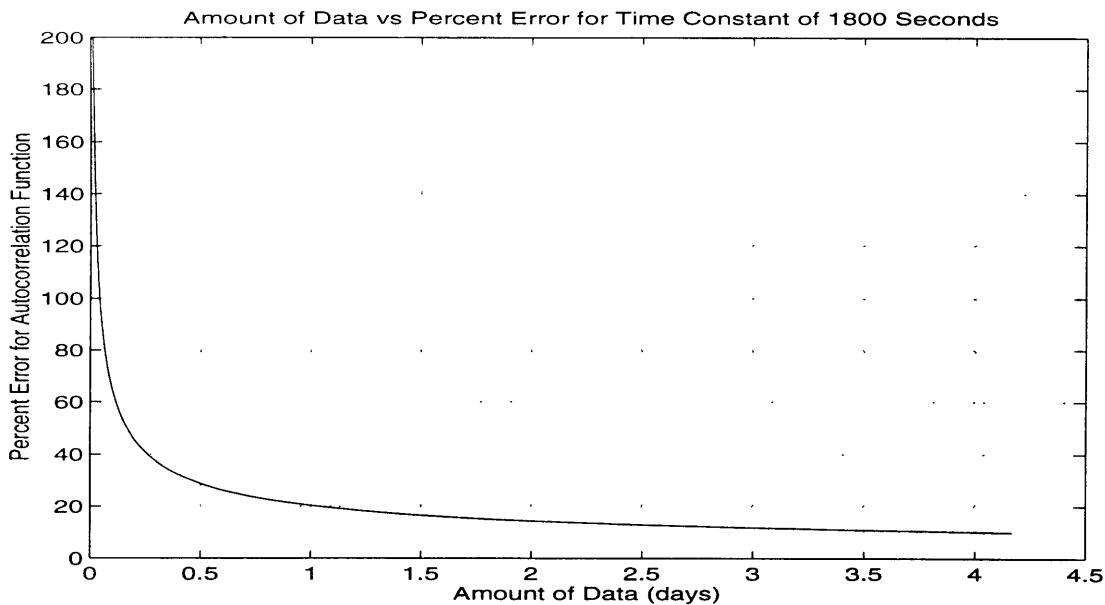


**Figure 3.2 Amount of Data vs. Percent Error**

obtain about 10% error on the autocorrelation function. For our problem, we must have data where the satellites are all the same for each set of data. This limits the data sets to about one hour before a satellite switch occurs. The second reason for abandoning correlation as the analysis method was that it does not easily allow the resolution of multiple Markov processes. It will be found that there were indeed two separable Markov processes with, obviously, different time constants.

### **3.5 Time Delay Error Analysis**

An alternative method for observing and characterizing the error inherent in using a time delayed DGPS correction was developed. It consisted of simply computing the time delay differences as a function of time delay and fitting those differences to a presumed model. The time shift ranged from zero to a maximum such that 20 data points remained in common between the original set and the shifted set. Since the data interval was 10 seconds, this corresponds to an overlap of 200 seconds. Thus a 1500 sec-

ond data set will yield a 1300 second set of time shifted differences. The differences are the mean square, MS, of the components of the RMS differences at each time shift.

After each shift, the shifted and unshifted errors were differenced. The differences (at each overlapping point) are functions of the total shift,  $\tau$ . (A shift by an index of one corresponds to a 10 second shift.) For the discrete case these differences are

$$x_{\text{diff}_{i,m}} = x_{\text{err}_{i+m}} - x_{\text{err}_i} \quad (3.9)$$

The mean and standard deviation at each shift,  $m$ , was found by summing over  $i$

$$\bar{x}_{\text{diff}_m} = \frac{\sum_i x_{\text{diff}_{i,m}}}{n_m} \quad (3.10)$$

$$\overline{x^2}_{\text{diff}_m} = \frac{\sum_i x_{\text{diff}_{i,m}}^2}{n_m} \quad (3.11)$$

where the sum on  $i$  is over the number of overlapping points,  $n_m$ , at each shift,  $m$ .

The mean square, MS, of the  $x$ ,  $y$ ,  $z$  standard deviations was computed

$$\text{diff}_{\text{MS}}^2(\tau) = \overline{x^2}_{\text{diff}_m} + \overline{y^2}_{\text{diff}_m} + \overline{z^2}_{\text{diff}_m} \quad (3.12)$$

where the mean square difference is expressed in terms of the time delay,  $\tau$ , corresponding to the shift,  $m$ .

Figure 3.3 shows this process in block diagram form. The result of the time delay error process is a curve of mean square error for differences vs.  $\tau$ .

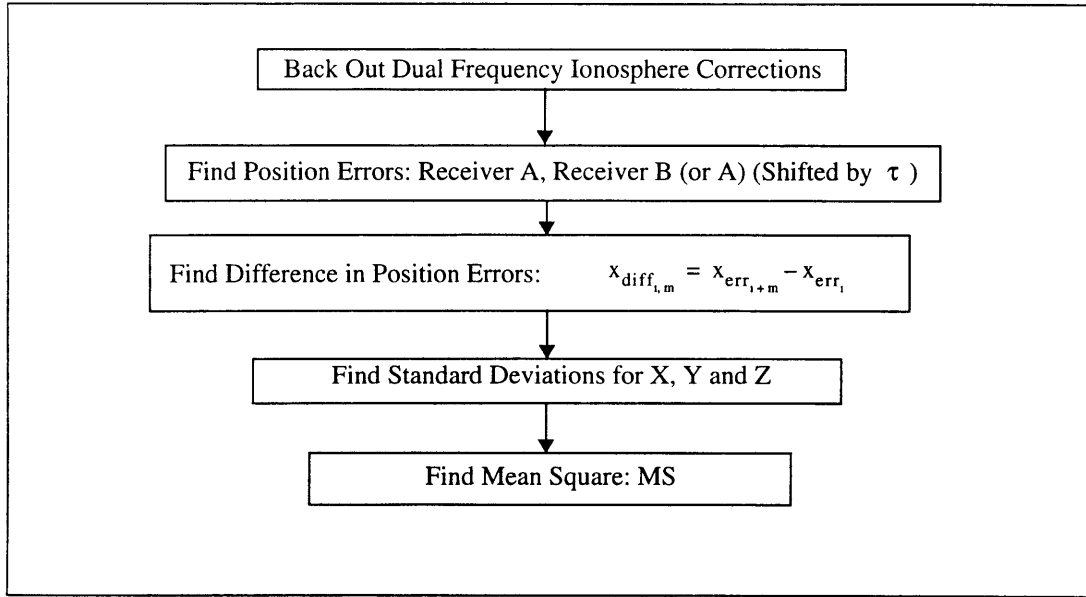


**Figure 3.3 Creating Time Delay Errors**

### 3.6 Relation of Mean Square Differences to Markov Model

Consider the outputs of receiver A and B:  $(x_A, y_A, z_A)$  and  $(x_B, y_B, z_B)$ . Taking the RSS of each provides  $RSS_A$  and  $RSS_B$  as in Equation (3.10). The difference is  $DIFF = RSS_A - RSS_B$ . The variance on the difference is given by

$$\sigma_{DIFF}^2 = \overline{DIFF^2} - \overline{DIFF}^2 \quad (3.13)$$

If the difference is a zero mean process, then

$$\sigma_{DIFF}^2 = \overline{DIFF^2} = \overline{RSS_A^2} - 2\overline{RSS_A RSS_B} + \overline{RSS_B^2} \quad (3.14)$$

Assume both A and B are zero mean processes, then  $\overline{RSS_A^2} = \sigma_A^2$ ,  $\overline{RSS_B^2} = \sigma_B^2$ , and  $\overline{RSS_A RSS_B} = \rho\sigma_A\sigma_B$ . This leads to

$$\sigma_{DIFF}^2 = \sigma_A^2 - 2\rho\sigma_A\sigma_B + \sigma_B^2 \quad (3.15)$$

Assuming A and B have similar variances,  $\sigma_A^2 = \sigma_B^2 = \sigma_{AB}^2$  resulting in Equation (3.16).

$$\sigma_{\text{DIFF}}^2 = 2\sigma_{AB}^2 - 2\rho\sigma_{AB}^2 = 2\sigma_{AB}^2(1 - \rho) \quad (3.16)$$

Letting  $\rho = e^{-\frac{t}{\tau} - \frac{x}{x_c}}$  for a Markov process leads to the model function

$$\sigma_{\text{DIFF}}^2 = 2\sigma_{AB}^2 \left( 1 - e^{-\frac{t}{\tau} - \frac{x}{x_c}} \right) \quad (3.17)$$

which is equivalent to the mean square error if the bias is zero.

### 3.7 Marquardt Method

The Marquardt Method is a non-linear curve fitting routine that enables the fit of an exponential to a set of data. This is the means of obtaining the estimates for the DGPS model parameters. The inputs to the model include arrays of the independent and dependent data points, along with the standard deviations for each data point. The algorithm determines the standard deviation and correlation constant for the first order Markov fit, along with a covariance matrix that can be used to generate error bounds for the model.

The process defines a chi-squared ( $\chi^2$ ) merit function and determines best-fit parameters by minimizing the merit function. For the nonlinear case, the minimization is performed iteratively. The procedure is repeated until  $\chi^2$  effectively stops decreasing. The selected limit for the difference between consecutive  $\chi^2$  values was 0.1. [22] The Marquardt method is described in more detail in Appendix A. The Marquardt method is used to determine independently the errors due to baseline distance and time delay.

### 3.8 Pseudorange Error Processing

All previous processing was performed using the navigation solutions that are provided by the GPS receiver. Due to the satellite switches, the data sets are limited in length. In an effort to obtain longer data sets, the possibility of obtaining pseudorange errors was investigated. The pseudorange from a single satellite could cross over several satellite switches and provide a source of continuous data for use in the processing.

Equation (3.18) is used to obtain the pseudorange errors.

$$\rho_{\text{meas}} - \rho_{\text{true}} = \mathbf{H} \begin{bmatrix} \mathbf{r}_{\text{meas}} - \mathbf{r}_{\text{true}} \\ \Delta t_{\text{meas}} - \Delta t_{\text{true}} \end{bmatrix} \quad (3.18)$$

where  $\mathbf{H}$  is given by Equation (3.19).

$$\mathbf{H} = \begin{bmatrix} \mathbf{u}_1^T & 1 \\ \mathbf{u}_2^T & 1 \\ \mathbf{u}_3^T & 1 \\ \mathbf{u}_4^T & 1 \end{bmatrix} \quad (3.19)$$

The line of sight vector to each satellite is given by  $\mathbf{u}_i^T$ . The vector  $\rho_{\text{meas}}$  contains the measured pseudorange for each of the four satellites. The output GPS navigation solution vector is  $\mathbf{r}_{\text{meas}}$ . The receiver's true position vector is  $\mathbf{r}_{\text{true}}$ . The user clock bias estimate is  $\Delta t_{\text{meas}}$ . The true user clock bias is  $\Delta t_{\text{true}}$ . The line of sight vector to each satellite is obtained by using post-processed ephemeris data downloaded from the Internet. The ephemeris data is obtained at 15 minute intervals, and an interpolation routine called `polint.m` is used to find the true ephemeris for all data points [22].

The problem with the pseudorange processing is that while we have a value for  $r_{\text{true}}$ , the true clock bias in Equation (3.18) is not known. If the error in the user clock bias,  $\Delta t_{\text{meas}} - \Delta t_{\text{true}}$ , is forced to be zero, the pseudorange errors obtained will have jumps in them at each satellite switch. This is shown in the top half of Figure 3.4. If this jump is attributed to the change in  $\Delta t_{\text{meas}}$  due to the satellite switch, a correction term can be obtained which indeed allows the three continuing pseudoranges to be continuous. An example is shown in the bottom half of Figure 3.4.

The actual clock error, however, is still unknown. We have simply found the change in its estimate due to the satellite switch. The difference between the measured and true clock error is a contributor to the pseudorange error, and cannot be ignored. It

may however be possible to estimate the contribution of this term statistically based on the TDOP. This will be discussed in Section 5.2.

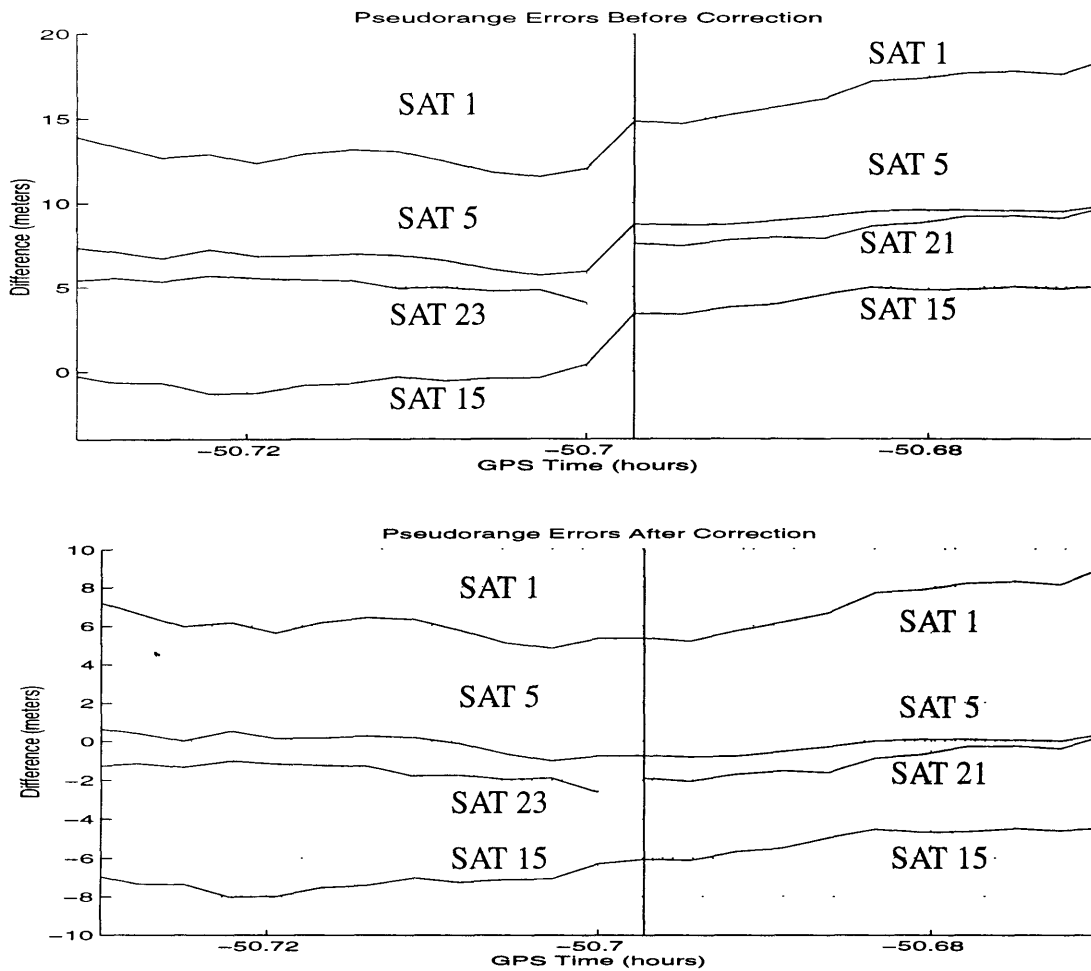


**Figure 3.4 Breaks in Pseudorange Errors**

### 3.9 Multipath

As GPS signals are reflected off objects before entering the receiver antenna, a false pseudorange is created. This happens because the reflected signal has traveled a different path length than the direct signal. As noted in the previous section, cyclic behavior can be observed in the GPS position output which may be attributable to this “multipath” effect.

Oscillations are also observed in the time delay errors formed by shifting one receiver's data in time and differencing this with the other receiver's output. Figure 3.5 illustrates the point by showing the time delay error results from six data sets in the zero baseline case. Note the oscillations that occur in each set.

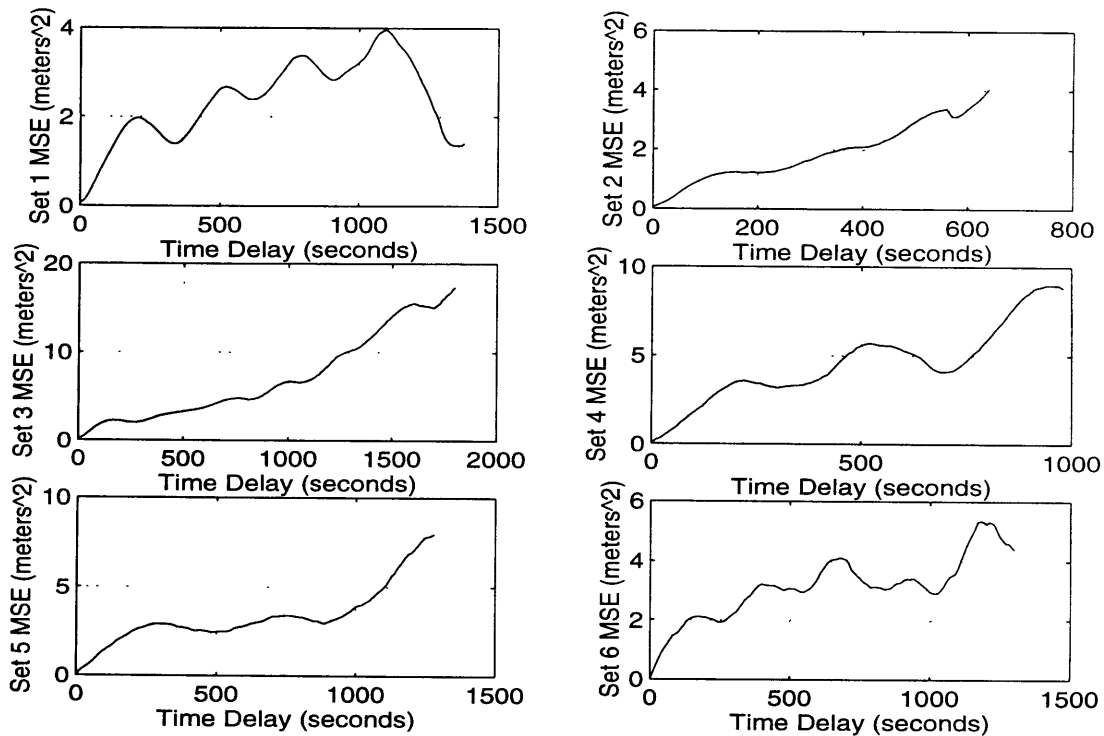


**Figure 3.5 Oscillations in Time Delay Errors, Zero Baseline Data**

After noting similar frequencies in each set, the average period was identified by taking the fast Fourier transform (FFT) of each set shown. Figure 3.6 shows the FFT outputs from each of the six sets. The FFT output is very similar for all the sets with the tallest peaks occurring from 300 seconds to 600 seconds. Peaks off the scale were attributed to taking the FFT of a finite set of data. Peaks are expected to occur at 700 to 1500 seconds because that's how long the individual data segments lasted. The pre-



dominant periods which can reasonably be attributed to multipath are between 300 seconds and 600 seconds.

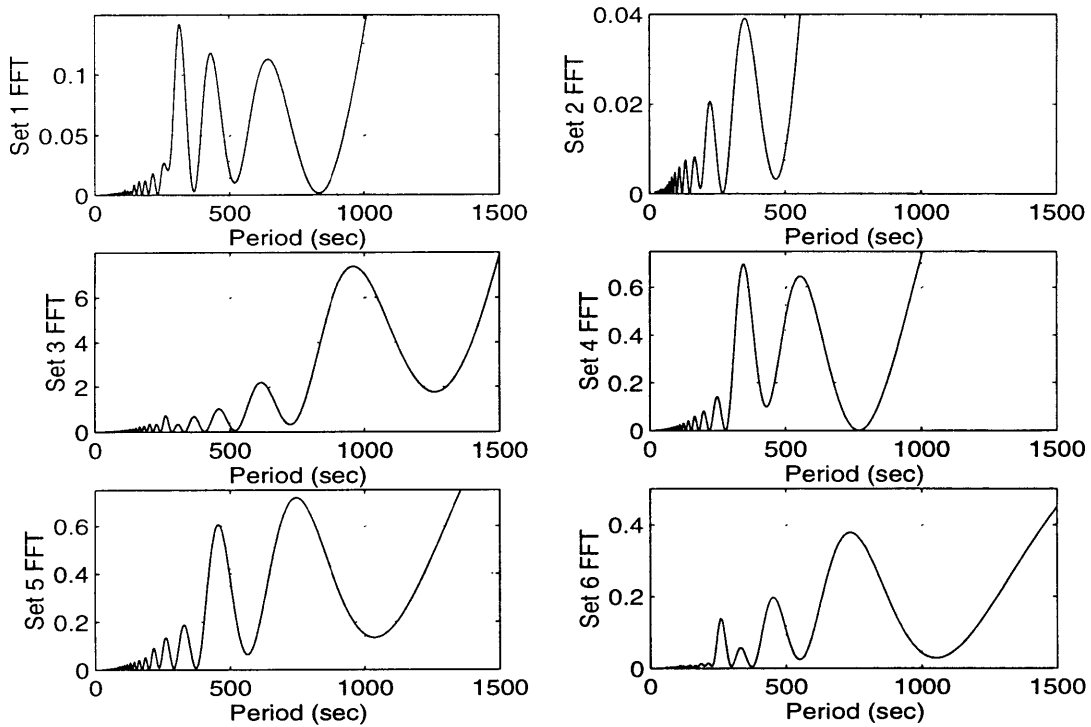


**Figure 3.6 FFT of Time Delay Errors, Zero Baseline Data**

A scenario was developed which results in the multipath frequencies observed for the satellites in the zero baseline, 5-hour data set. The user selects a position offset

from the receiver for the location of the reflector. The true range and satellite position are used to determine the multipath frequency. The scenario is shown in Figure 3.7.

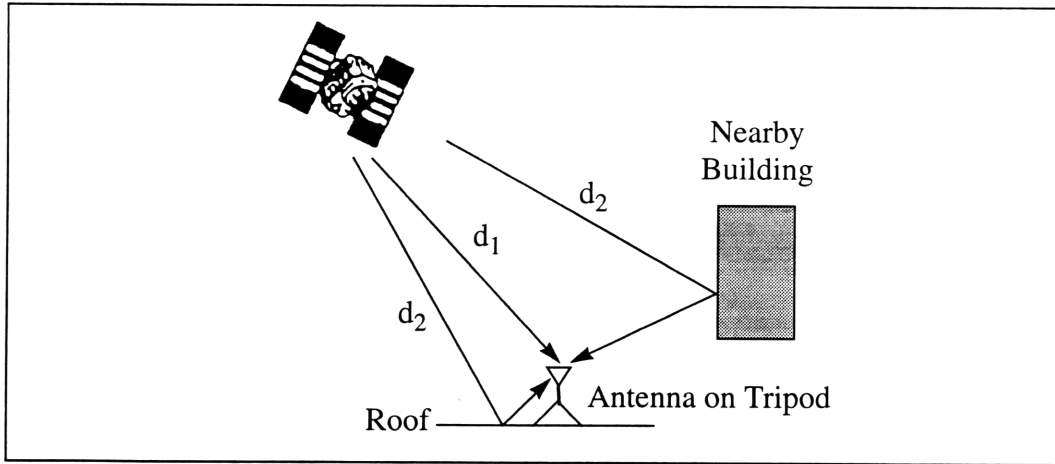


**Figure 3.7 Signal Multipath**

As shown,  $d_1$  is the direct path from satellite to receiver. Two possible reflective paths,  $d_2$ , were considered as examples. Note that  $d_2$  includes the path before and after the reflection or the total from the satellite to the antenna. One was a reflection off a nearby building. The position offset used was 20 meters north and 20 meters up. The second multipath option is a reflection off the roof that enters under the receiver. This case is highly likely because the antenna was on a tripod and the gain under the receiver is fairly high. The offset used for this case was 1.9 meters down and 0.5 meters north.

The multipath frequency is given in Equation (3.20) and Equation (3.21).

$$f(k) = \frac{\Delta d_1}{\lambda \Delta t} - \frac{\Delta d_2}{\lambda \Delta t} \quad (3.20)$$

$$f(k) = \frac{d_1(k+1) - d_1(k)}{0.19(t(k+1) - t(k))} - \frac{d_2(k+1) - d_2(k)}{0.19(t(k+1) - t(k))} \quad (3.21)$$

where  $\lambda$  is the wavelength of the signal (0.19 meters),  $t$  is the measurement time, and  $k$  is the index for the measurements. The results for satellite 26 for the first offset are

shown in Figure 3.8. The period is between 90 and 100 seconds (1.5 to 1.7 minutes), and the frequency is 0.0095 to 0.011 Hz.

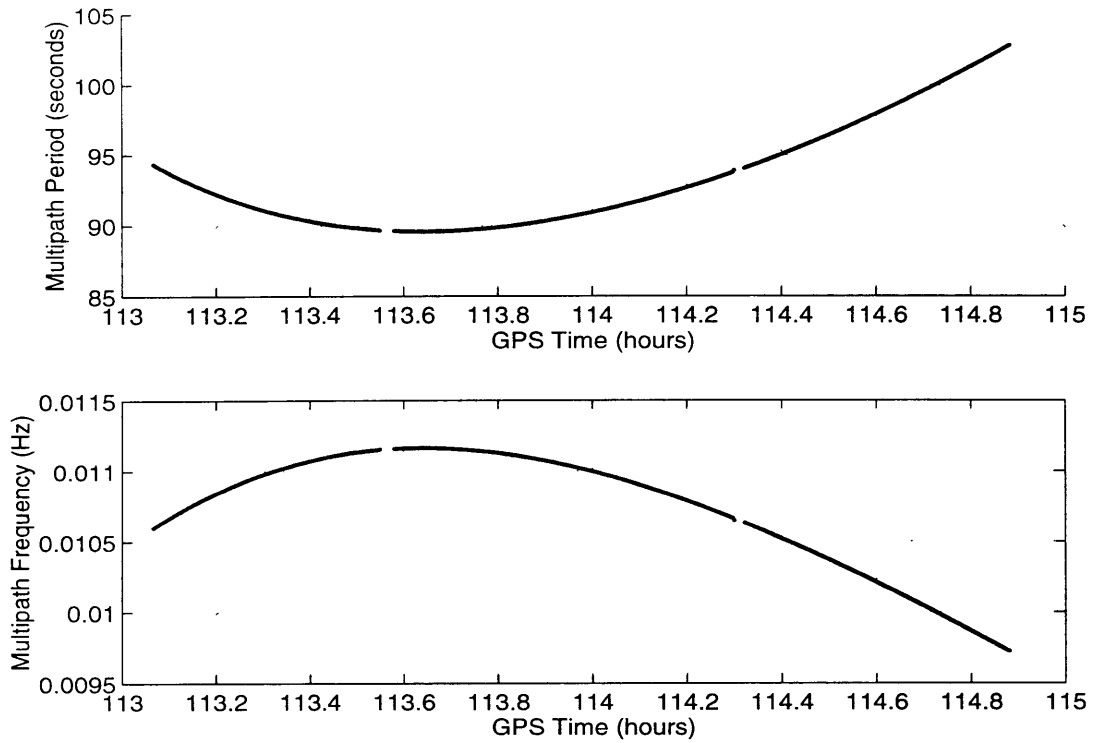


**Figure 3.8 Sample Multipath Period for Offset of 20 Meters**

Figure 3.9 shows the results for the reflections under the antenna. The period in this case is 150 seconds or greater (1.5 - 10 minutes), and the frequency is 0.008 Hz or less.

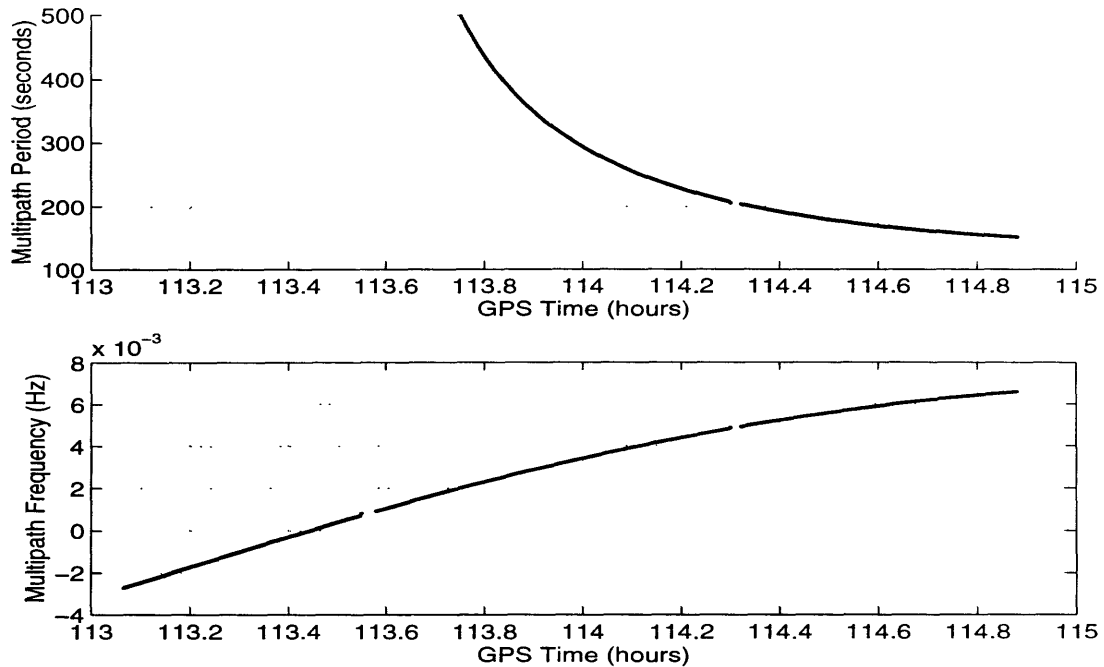


**Figure 3.9 Sample Multipath Period for Offset of 1.9 Meters**

Experimental observations of multipath were found in [1, 16]. Multipath frequencies with time periods of 5 to 30 minutes were recorded. Differential multipath with time periods of 5 to 10 seconds were observed. The simulation results are in the range of these observations. Other multipath “paths” are possible. The two examples were only intended to indicate reasonableness. No attempt was made to actually measure the distance to nearby buildings.

Note that the frequencies observed in the data and those found from the simulation of reflections from under the receiver fall into the same frequency range. The frequency for reflections off nearby buildings matches closer with the frequencies found in the raw data highlighted in the last section.

# Chapter 4

## Results

### 4.1 Rooftop Experiment Results

#### 4.1.1 Navigation Solution for 5-Hour Data

The first set of results is from processing the navigation solution for the 5-hour set of data with the zero baseline. Figure 4.1 shows the satellites that were used during the data collection. The y-axis is the satellite identification number. Note that at each time only four satellites are being used. The gap between 115 and 116.5 hours was noted earlier as the time when less than four satellites were tracked.

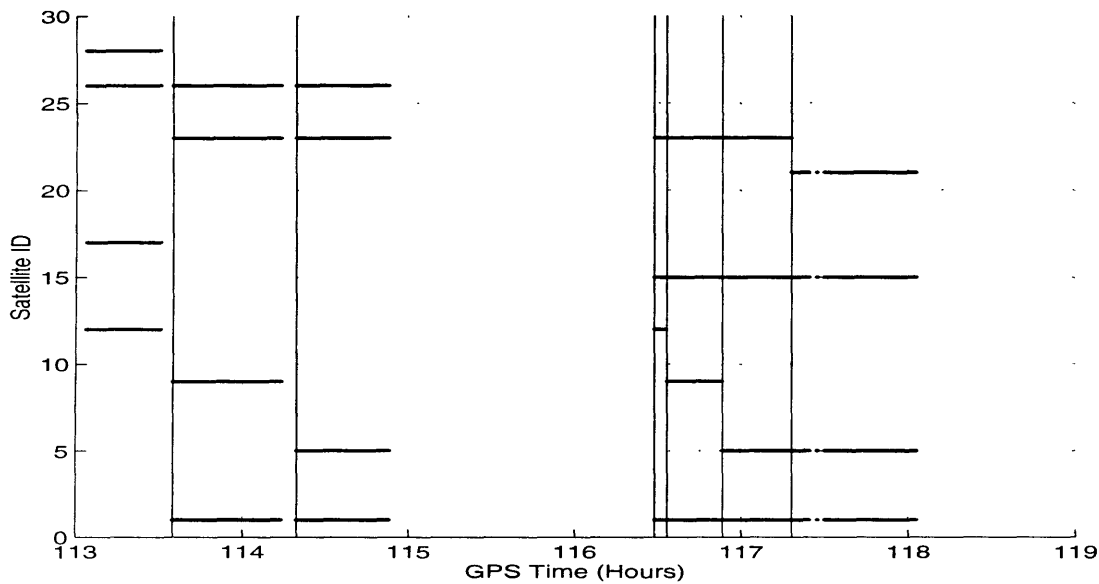
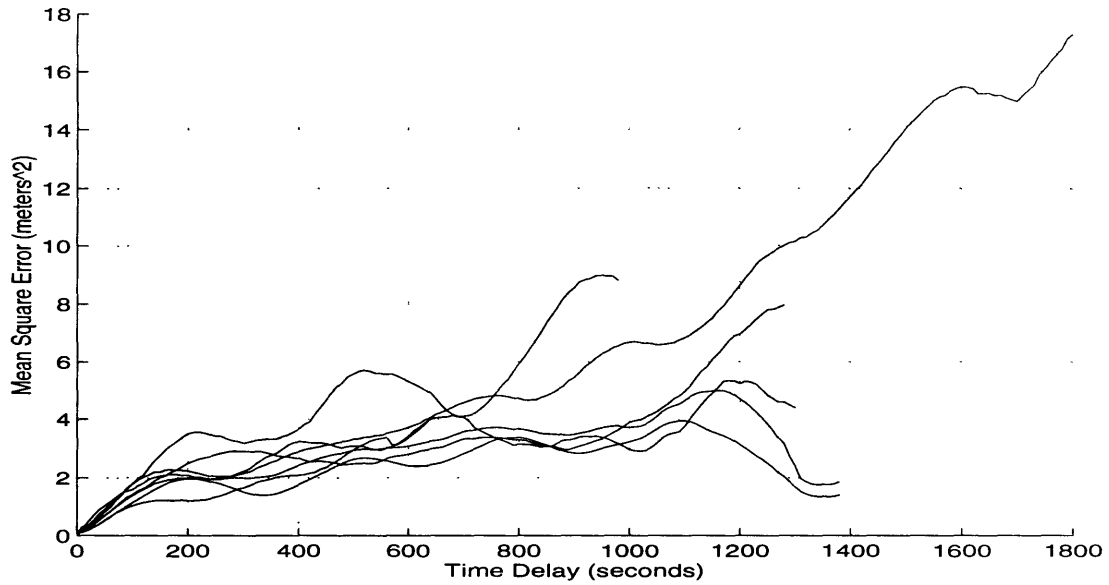


Figure 4.1 Satellite ID vs. Time

The vertical lines mark each spot where there is a switch in at least one of the satellites being tracked. The data was split into six different sets where the satellite set stayed constant over that interval. The small data segment towards the middle was not used.

Time delay differences were created using the processing described in Chapter 3. Figure 4.2 shows the resulting mean square vs. time delay plots for each of the six sets of data. The average is also plotted on this chart.



**Figure 4.2 Navigation Solution Errors**

Figure 4.3 shows the 1-sigma bounds on the time delay differences. These were computed by finding the standard deviation for the mean square error calculation as shown in Equation (4.1). [11] Note that the error bounds for the six sets overlap much of the time.

$$\sigma_{MS} = \sqrt{2\sigma_{RSS}^4 / (n_m - 1)} \quad (4.1)$$

where  $\sigma_{RSS}^2$  is the mean square error (ordinate in graph), and  $n_m$  is the number of overlapping points. It can be seen that the error bounds increase as the number of overlapping points decreases for increasing time delay.

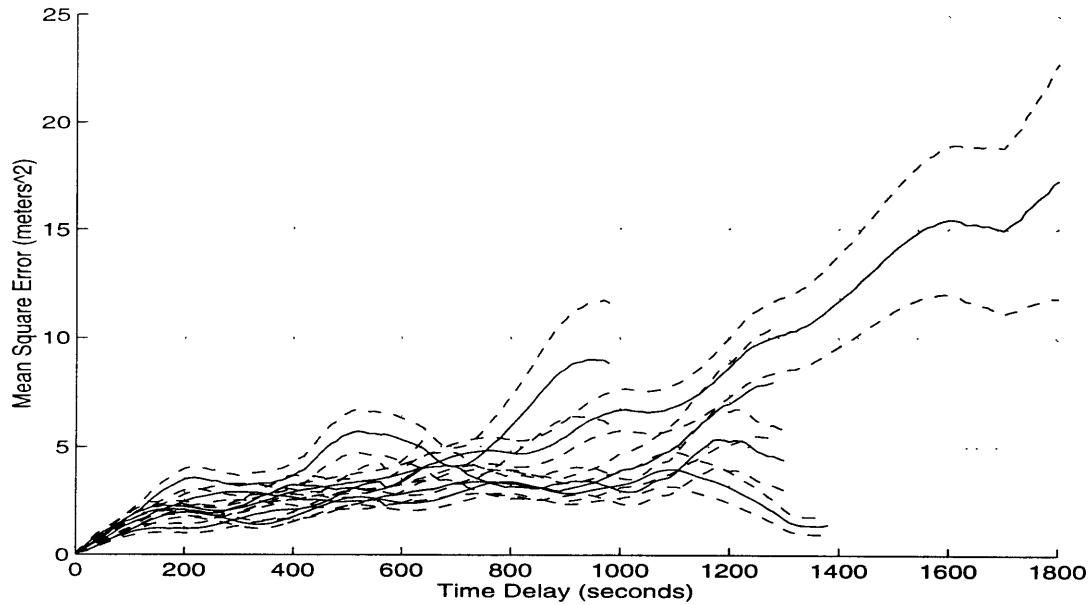


**Figure 4.3 One-Sigma Bounds for Time Delay Errors**

Figure 4.4 shows the weighted average from the six data sets, along with the standard deviation on the average. These values are used as inputs to the Marquardt curve fitting routine. The weighted average and standard deviation were found using Equation (4.2) and (4.3) where  $MS_i$  is the mean square for each set and  $\sigma_i$  is the standard deviation for the mean square.

$$\text{mean} = \frac{\sum_i \frac{MS_i}{\sigma_i^2}}{\sum_i \frac{1}{\sigma_i^2}} \quad (4.2)$$

$$\sigma_{\text{mean}} = \frac{1}{\sqrt{\sum_1 \frac{1}{\sigma_1^2}}} \quad (4.3)$$

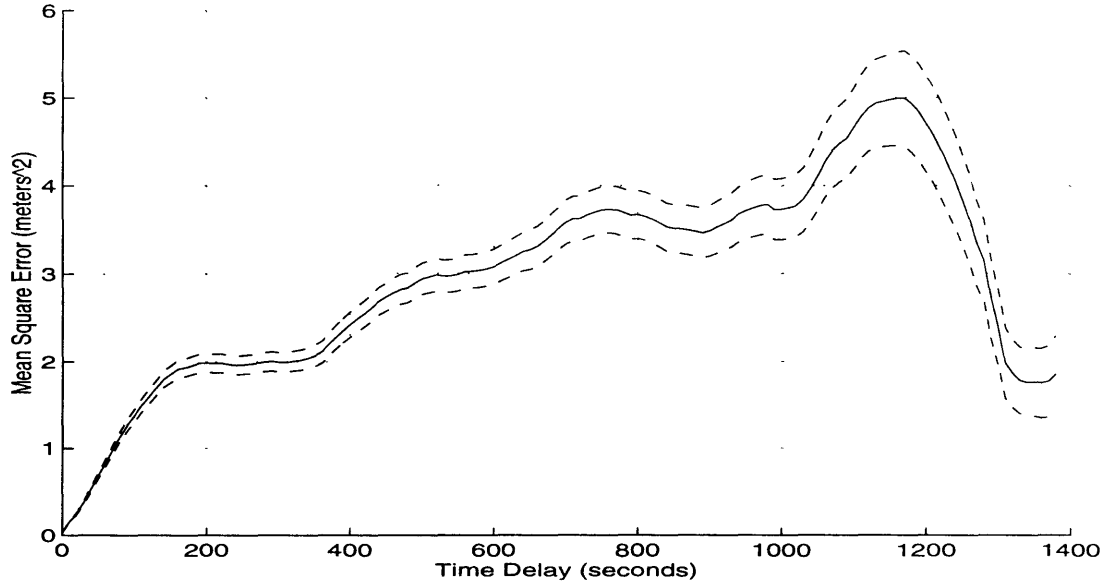


**Figure 4.4 Average Navigation Solution Error**

Figure 4.5 shows the Markov fit to the average from the 6 data sets. Equation (4.4) shows the model that was used in the Marquardt fitting routine. A sum of two Markov processes was used because this model provided a better fit to the data. The first process with the shorter time constant is attributed to multipath. The period falls in the sample range found in the multipath scenario as discussed in Chapter 3. All the zero baseline cases exhibit this short time constant behavior. The longer time constant process is intended to encompass all other errors. A model for this process was one of the goals of the study.

$$\text{Model} = \sigma_1^2 \left( 1 - e^{-\frac{t}{\tau_1}} \right) + \sigma_2^2 \left( 1 - e^{-\frac{t}{\tau_2}} \right) \quad (4.4)$$



The error bounds on the Markov fit are shown with dotted lines. These are obtained by using the covariance provided by the Marquardt routine as shown in Equation (4.5).

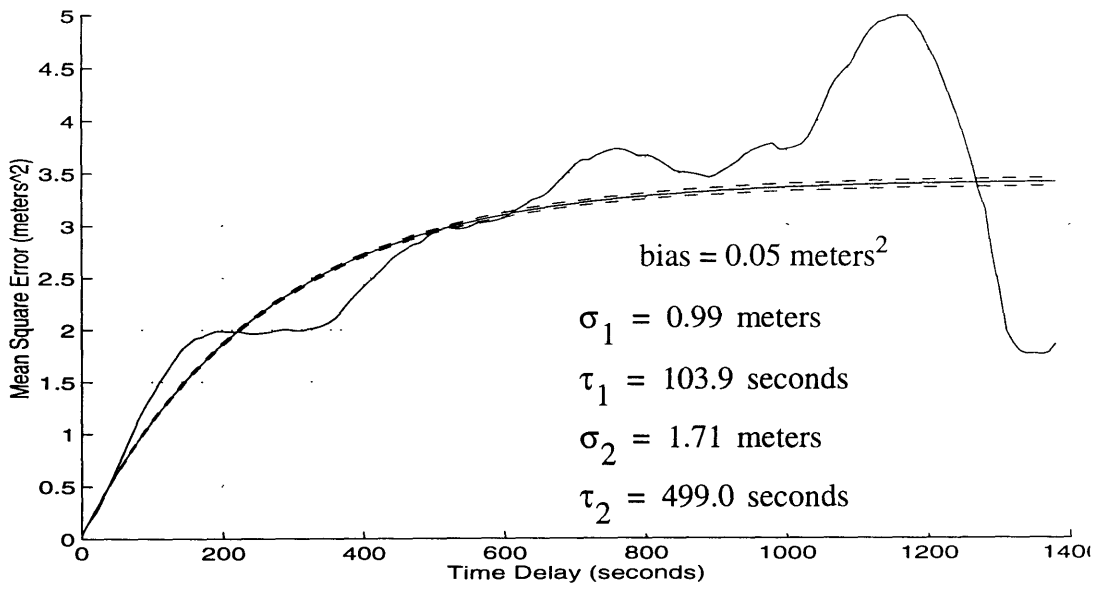
$$\delta e = \sqrt{\frac{\partial f}{\partial \bar{s}} E \frac{\partial f}{\partial \bar{s}}^T} \quad (4.5)$$

The one-sigma error on the model is  $\delta e$ . The function  $f$  is the mean square error which is a function of the vector  $\bar{s}$ . The vector  $\bar{s}$  consists of both values for  $\sigma$  and  $\tau$ . The partial derivatives of the function  $f$  with respect to the elements of  $\bar{s}$  are output from the Marquardt routine. The routine also provides the covariance matrix  $E$  defined by Equation (4.6).

$$E = \overline{\delta \bar{s} \delta \bar{s}^T} \quad (4.6)$$

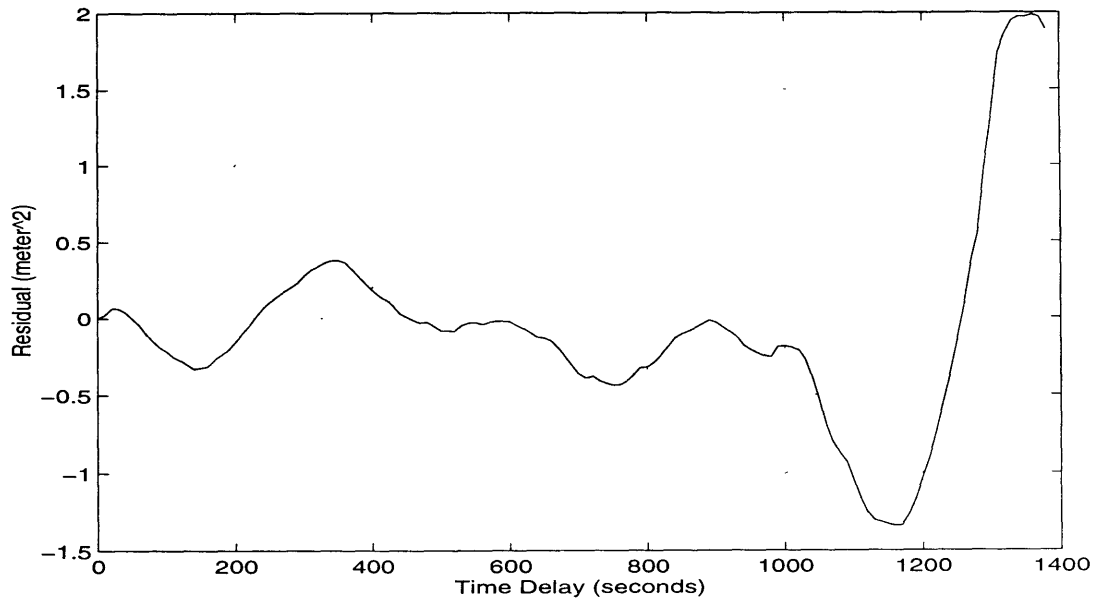
The noise level for the difference between receiver A and B is 0.05 meters<sup>2</sup> and provides a bias for the navigation solution errors. The receiver noise has a mean of 0.21 meters and a standard deviation of 0.23 meters. Squaring the standard deviation gives a bias for the mean square of 0.05 meters<sup>2</sup>.

Figure 4.6 shows the residual for the Markov process fit. This is obtained by subtracting the fit from the data. The residual represents anything that has not been



**Figure 4.5 Markov Process Fit**

included in the model. Note the sinusoidal characteristic in the residual. This will be addressed later in the chapter.



**Figure 4.6 Residual for Markov Fit**

The model parameters for each of the 6 sets and the average are given in Table 4.1. The average values are obtained from a separate fit for the average curve, not just the average for the parameter values from the 6 data sets. The fits to the individual sets reveal the fact that the Markov model is not very sensitive to changes in the  $\tau_2$  value. That is the reason for the large variations seen in this parameter. This insensitivity is related to the limit (variance) of the experimental correlation given in Chapter 3.

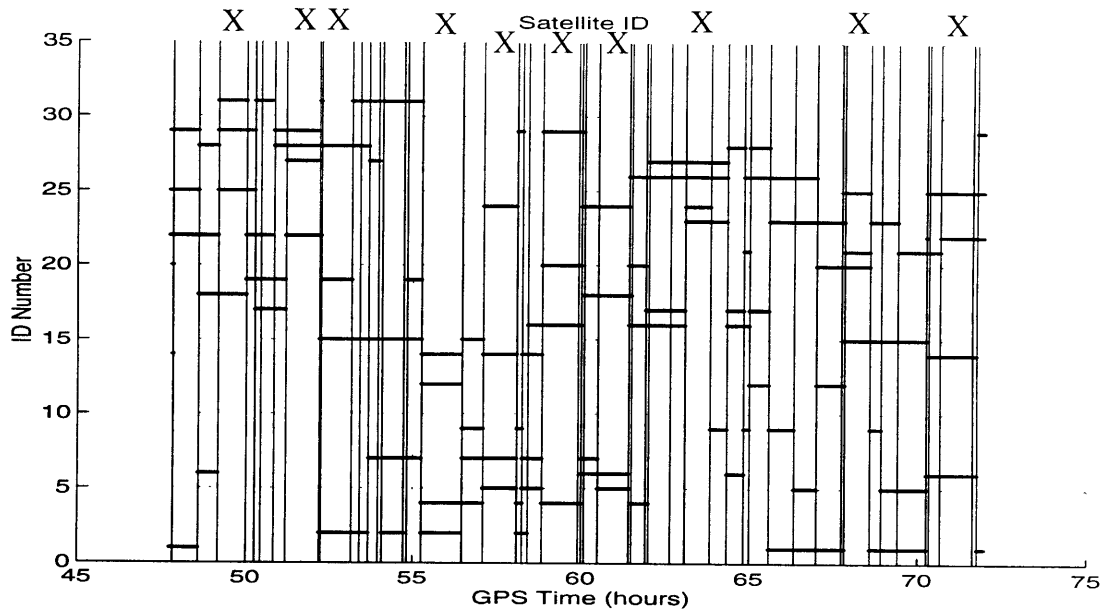
**Table 4.1 Results for Zero Baseline**

SET	$\sigma_1$ (meters)	$\tau_1$ (seconds)	$\sigma_2$ (meters)	$\tau_2$ (seconds)
1	1.25	272.5	1.02	285.9
2	0.68	80.2	5.74	7643.3
3	0.85	39.8	26.4	123,719
4	1.86	204.9	5.80	11,412
5	1.47	125.2	3.92	10,110
6	1.10	57.6	1.66	506.6
Average	0.98	103.9	1.71	499.0

#### 4.1.2 Navigation Solution for 24-Hour Data

The second set of results is from processing the navigation solution for the 24-hour set of data with the zero baseline. Figure 4.7 shows the satellites that were used during the data collection. The y-axis is the satellite identification number. Note that at each time only four satellites are being used. The vertical lines mark each spot where there

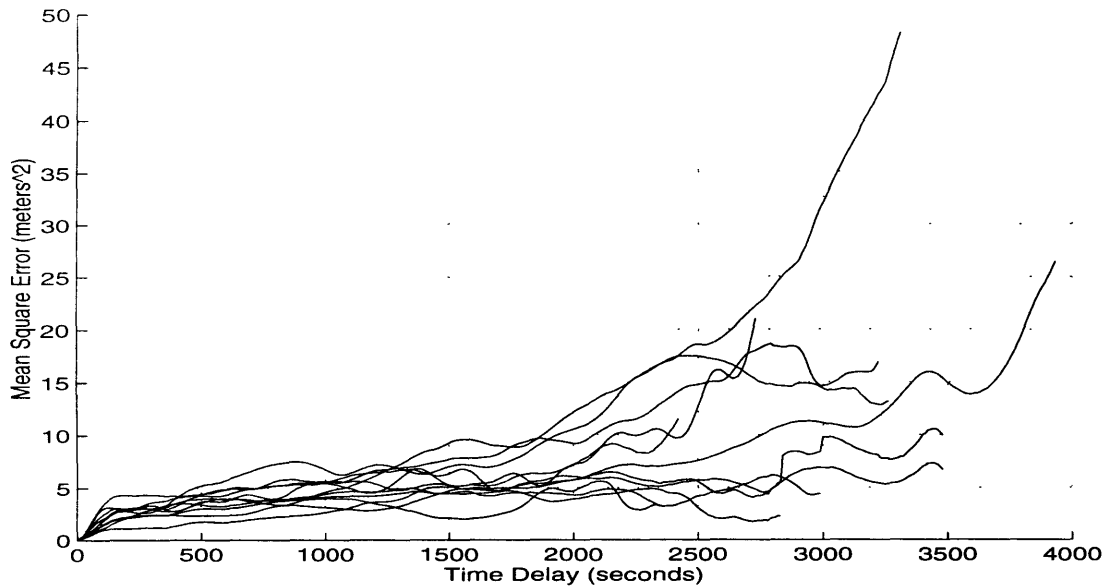
is a switch in at least one of the satellites being tracked. Ten sections were selected for processing of the navigation solution. These are indicated by an 'X' above the data set.



**Figure 4.7 Satellite ID, 24-Hour Data**

Time delay differences were created and Figure 4.8 shows the resulting mean square vs. time delay plots for each of the ten sets of data. The average is also plotted

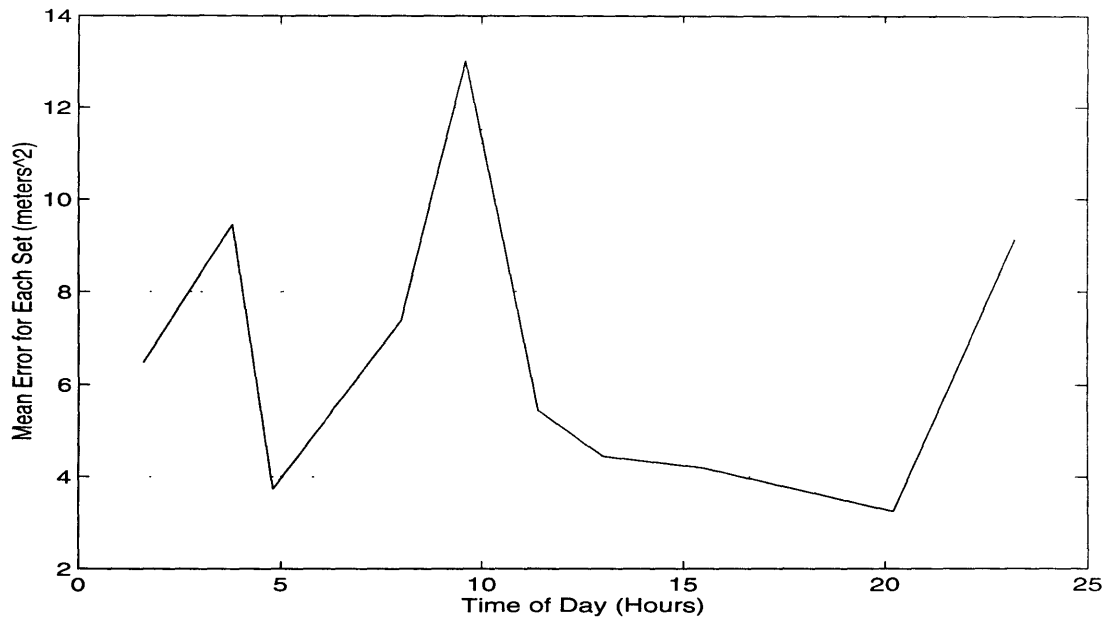
on this chart. The average is the very thin line that runs through the middle of the curves.



**Figure 4.8 Navigation Solution Errors, 24-Hour Data**

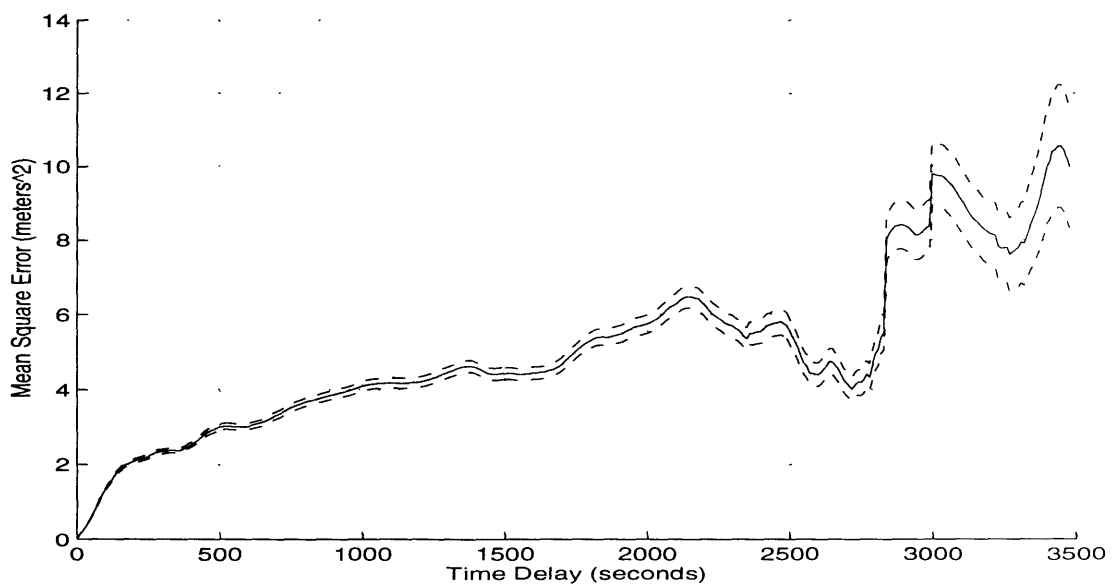
Noting that some of the curves in Figure 4.8 are lower than others, the time of day for each curve and the mean MSE were calculated. Figure 4.9 plots the mean of each of these sets of time delay differences versus time of day. The time of day is plotted from 0 to 24 hours (1 days). Hour zero occurs at midnight. It might be said that there is a large mean error between 8:00 a.m. and 10:00 a.m. corresponding to a rise in total electron count in the morning. the smallest mean square differences occur between noon and 8:00 p.m. There is then another increase. This increase occurs significantly

after sunset. Any correlation between the mean square differences and sunrise and sunset is difficult to discern.



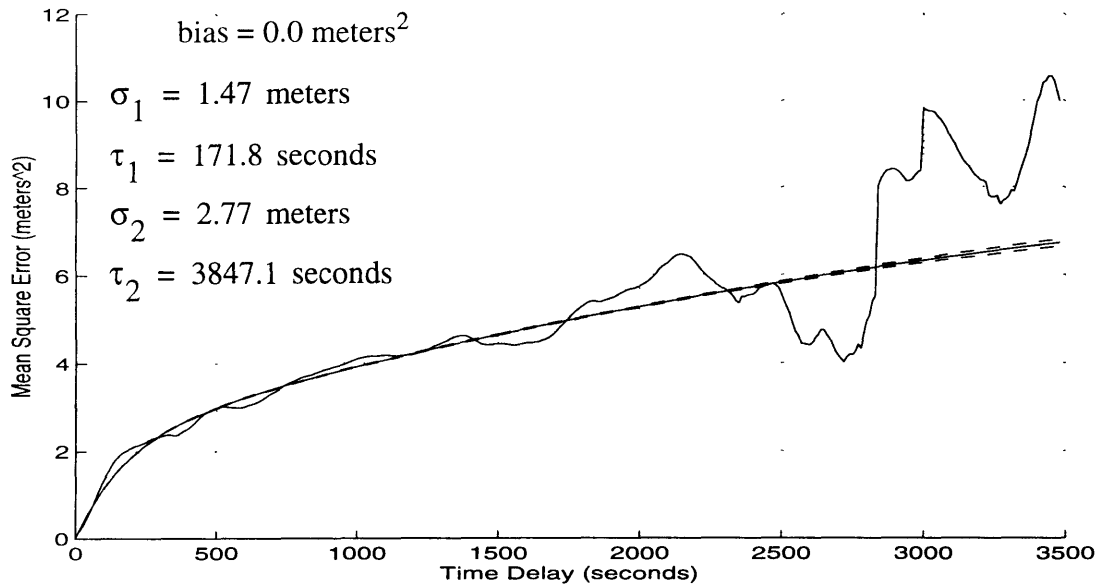
**Figure 4.9 Mean Error by Time of Day**

Figure 4.10 shows the average from the ten data sets, along with the standard deviation on the average. These values are used as inputs to the Marquardt curve fitting routine.



**Figure 4.10 Average Navigation Solution Error, 24-Hour Data**

Figure 4.11 shows the Markov fit to the average from the 10 data sets. The bias is zero because there is only one receiver for the 24-hour data. The result is a shift of receiver A vs. receiver A. The  $\tau_2$  value of 3847.1 seconds equals 1.07 hours.



**Figure 4.11 Markov Process Fit, 24-Hour Data**

Note that the error bounds on the raw data, Figure 4.10, and on the Markov fit, Figure 4.11, do not completely overlap. This is especially obvious after a few thousand seconds. This “inconsistency” reflects the fact that the Markov process is an incomplete description of the pseudorange transmission delay differences. In fact, the errors and their differences are not stochastic, but are “unpredictable”. Even this is not exactly the case because, with enough effort, satellite ephemeris and transmission delay could be predicted at least in the short term. Characterizing these differences as Markov processes is merely convenient. As the analysis proceeds the character of the fit residuals will be observed.

Figure 4.12 shows the residual for the Markov fit on the 24-hour data. Again note the sinusoidal nature of the model error.

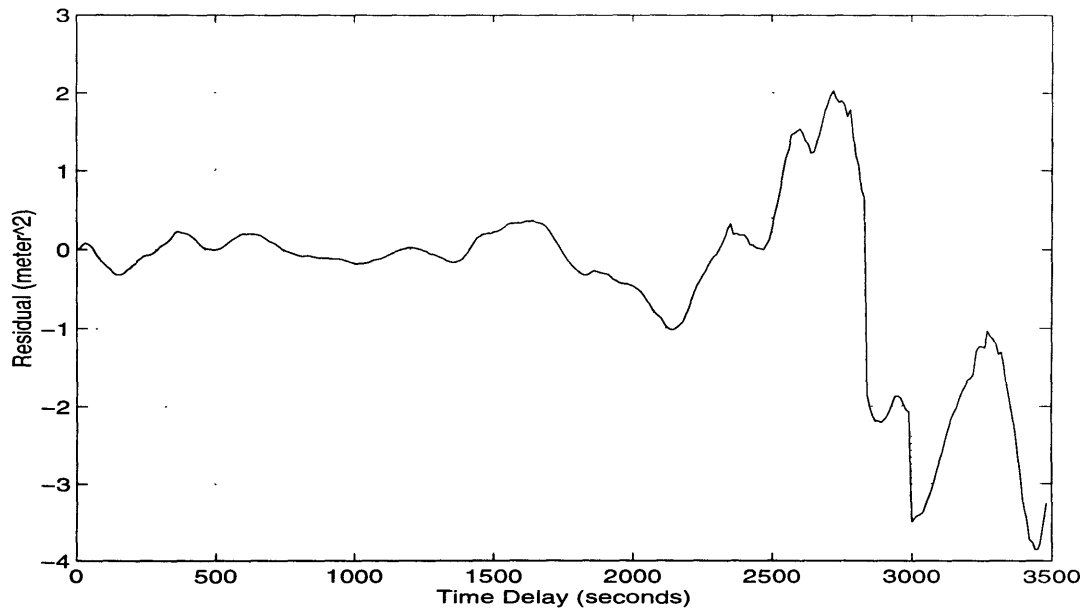


**Figure 4.12 Residual for Markov Fit, 24-Hour Data**

Figure 4.13 shows the Markov fit for both the 5-hour and 24-hour data sets. The model parameters for these two sets are almost identical. The data was collected on different days and times of day. The results indicate a definite consistency between the data sets. Note that at the end of each data set the average error increases sharply. This is a result of the fact that the number of data points is decreasing at each shift. The smaller segments have only 20 points left at the end, or only 200 seconds of data. It



seems reasonable that there would be trouble estimating a 1-hour time constant, with so few points remaining.

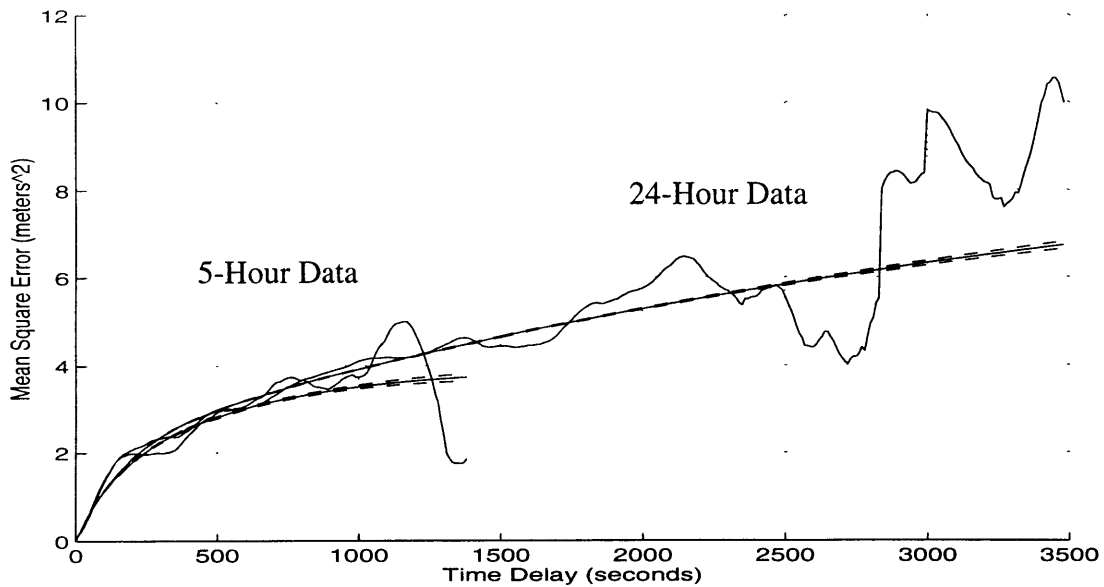


**Figure 4.13 Markov Process Fit, Both 5-Hour and 24-Hour Data**

The fit to each of the 10 navigation solution sets is given in Table 4.2. The large variance on the  $\tau_2$  values is again apparent, and we will note once more that it is consistent with the variance in the correlation given in Chapter 3.

**Table 4.2 Results for Zero Baseline, 24-Hour Data**

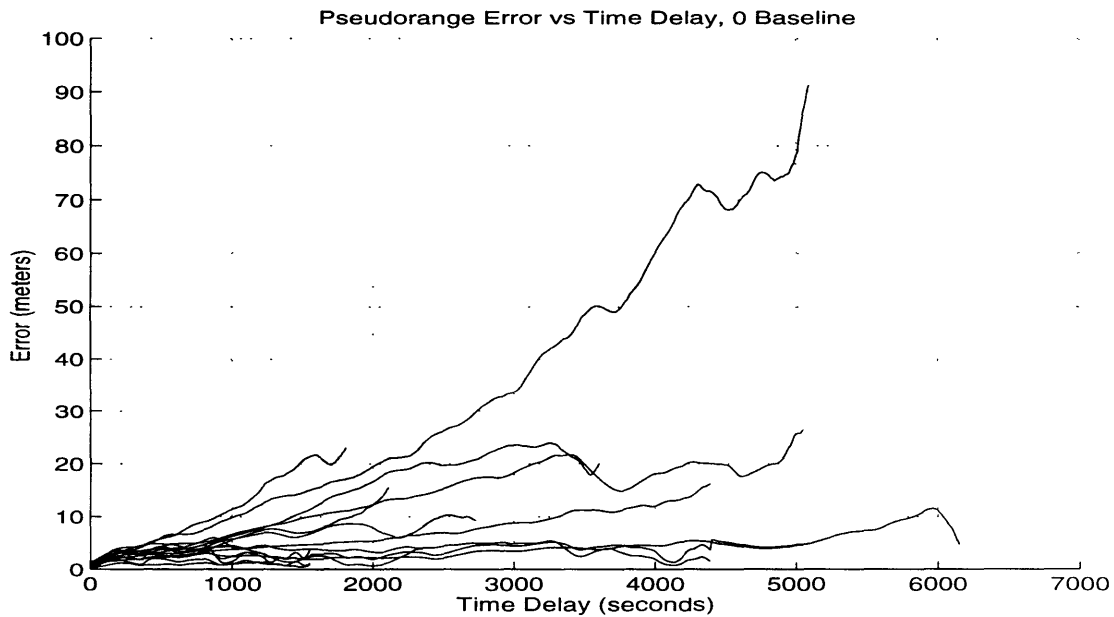
SET	$\sigma_1$ (meters)	$\tau_1$ (seconds)	$\sigma_2$ (meters)	$\tau_2$ (seconds)
1	1.57	89.8	9.51	38,358
2	1.81	255.0	12.54	45,316
3	1.50	208.6	1.27	214.0
4	1.07	123.1	41.4	$7.4 \times 10^5$
5	0.93	105.1	15.3	46,620
6	1.98	154.3	1.36	512.5
7	2.41	296.7	3.76	22,579
8	0.69	43.4	13.1	67,439
9	1.77	252.0	0.90	261.6

**Table 4.2 Results for Zero Baseline, 24-Hour Data**

SET	$\sigma_1$ (meters)	$\tau_1$ (seconds)	$\sigma_2$ (meters)	$\tau_2$ (seconds)
10	1.54	120.1	32.1	$2.7 \times 10^5$
Average	1.47	171.8	2.77	3847.1

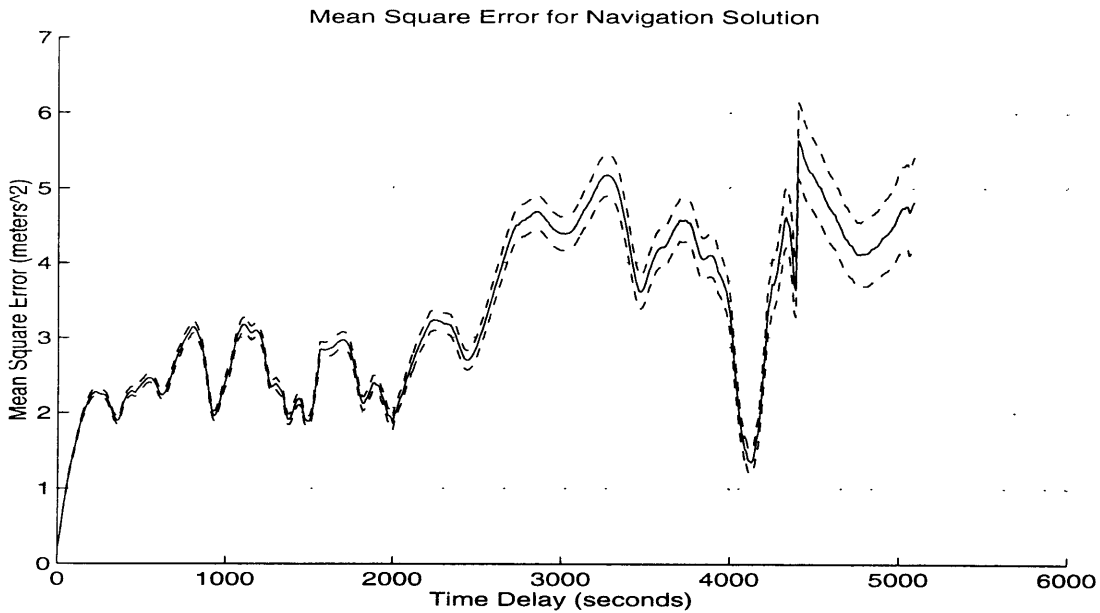
### 4.1.3 Pseudorange Errors, 5-Hour Data

The third set of results is from processing the pseudorange errors for the 5-hour set of data with the zero baseline. Fourteen pseudorange sequences were formed from the data. The large gap in the data forced the splitting of pseudoranges on either side of the gap. Figure 4.14 shows the resulting mean square vs. time delay plots for each of the fourteen sets of data. The average is also plotted on this chart.



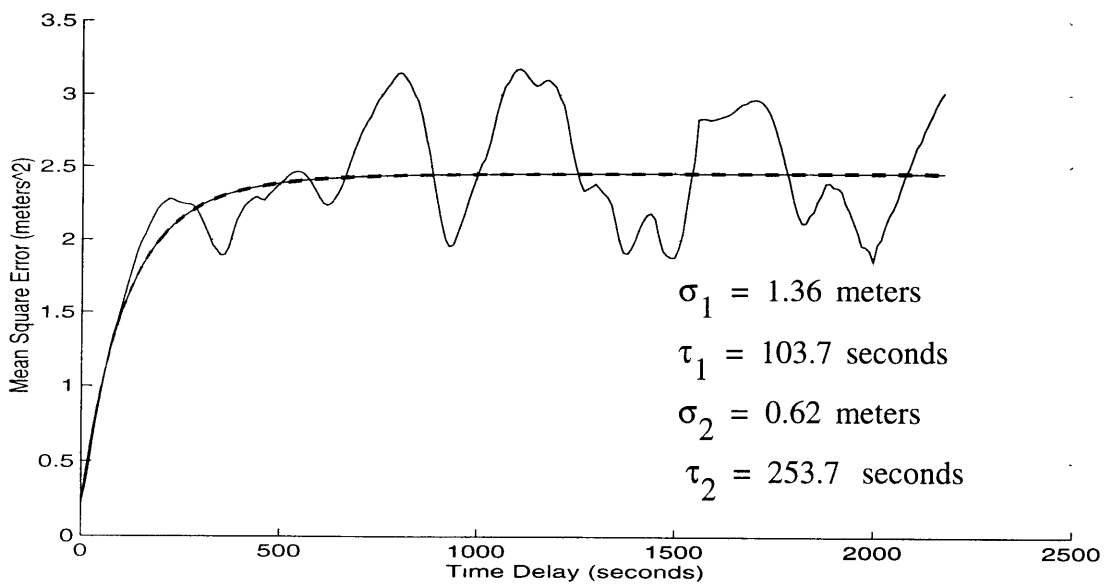
**Figure 4.14 Pseudorange Errors**

Figure 4.15 shows the average from the fourteen data sets, along with the standard deviation on the average. These values are used as inputs to the Marquardt curve fitting routine.



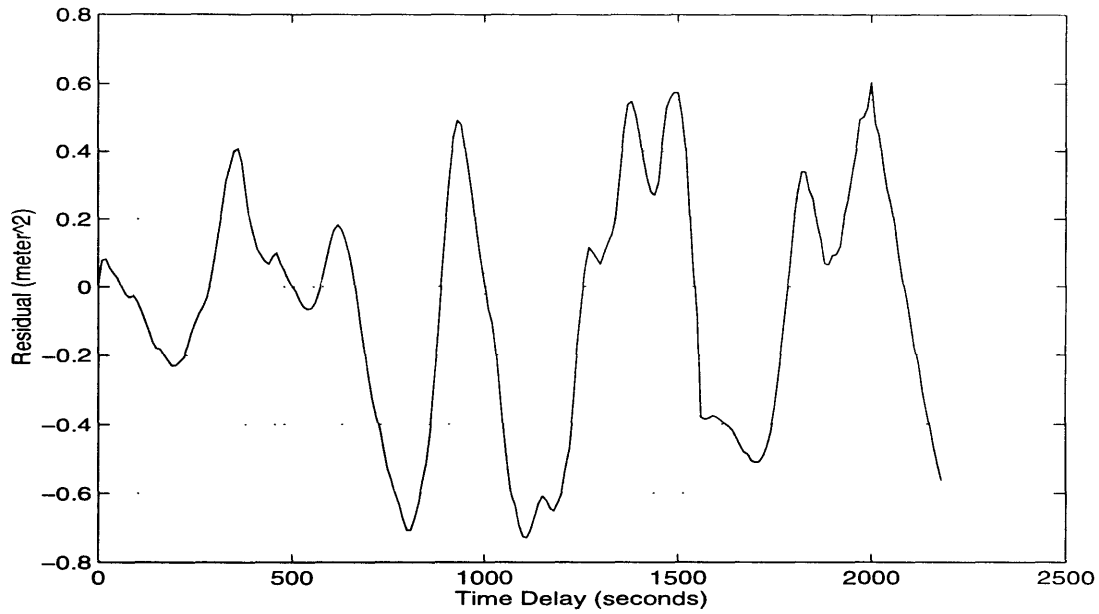
**Figure 4.15 Average Pseudorange Error**

Figure 4.16 shows the Markov fit to the average from the 14 data sets. The first rise is very close to what was seen in the navigation solution results.



**Figure 4.16 Markov Fit for Pseudorange Error**

The residual for the Markov fit is shown in Figure 4.17. Once again note the sinusoidal nature of the model error.

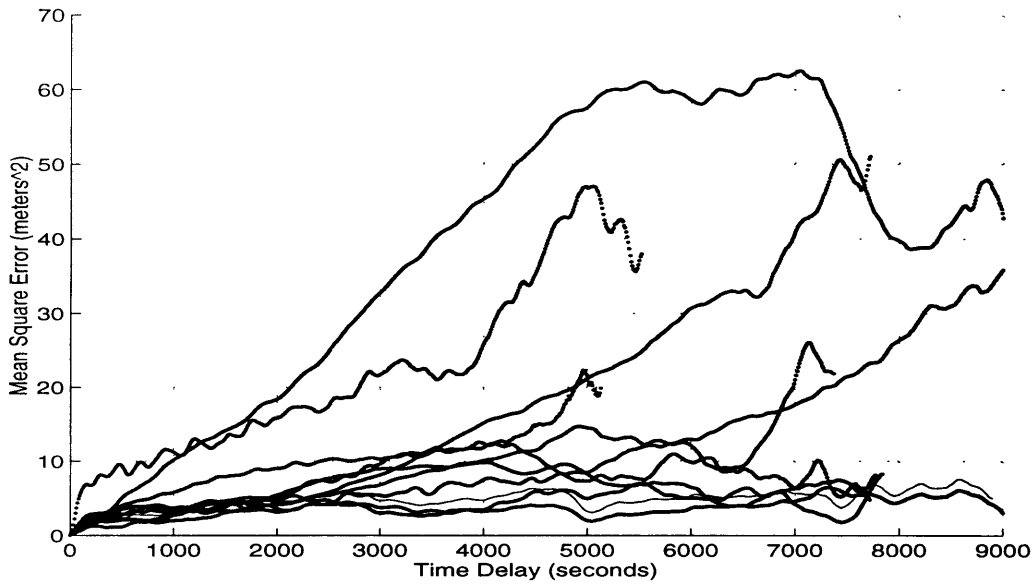


**Figure 4.17 Residual for Markov Fit, Pseudorange Errors**

#### **4.1.4 Pseudorange Errors, 24-Hour Data**

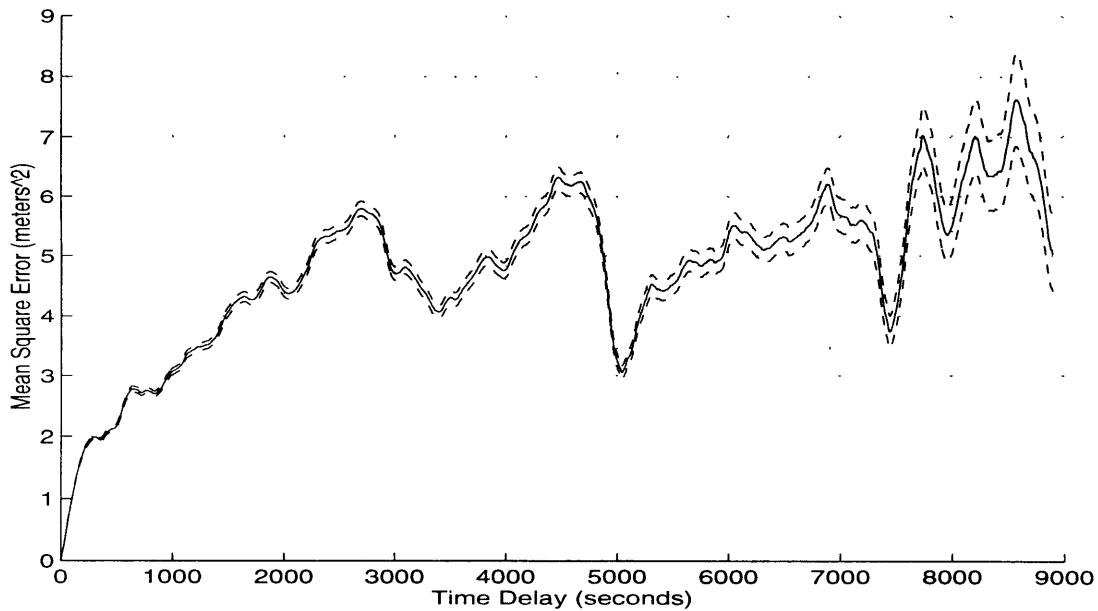
The fourth set of results is from processing the pseudorange errors for the 24-hour set of data with the zero baseline. Ten pseudorange sequences were formed from the

data. Figure 4.18 shows the resulting mean square vs. time delay plots for each of the ten sets of data. The average is also plotted on this chart.



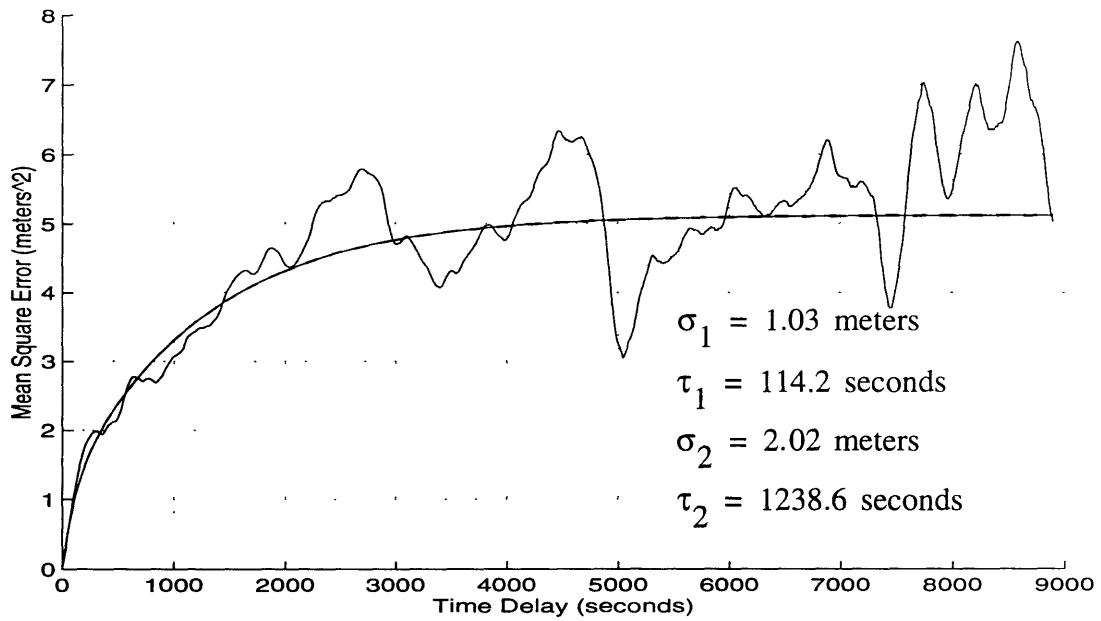
**Figure 4.18 Pseudorange Error, 24-Hour Data**

Figure 4.19 shows the average from the fourteen data sets, along with the standard deviation on the average. These values are used as inputs to the Marquardt curve fitting routine.



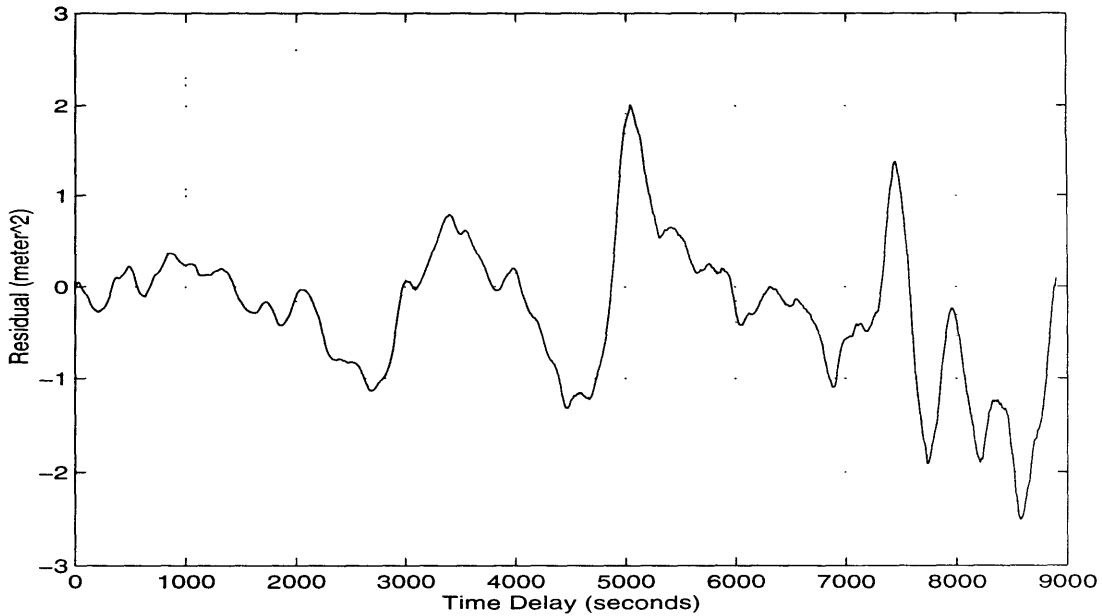
**Figure 4.19 Average Pseudorange Error**

Figure 4.20 shows the Markov fit to the average from the 14 data sets. Again, The first rise is very close to what was seen in the navigation solution results.



**Figure 4.20 Markov Fit for Pseudorange Error**

The residual for the Markov fit is shown in Figure 4.21. Once again note the sinusoidal nature of the model error.



**Figure 4.21 Residual for Markov Fit, Pseudorange Errors**

The Markov fit for all cases is shown in Figure 4.22. All the curves are aligned in the first rise.

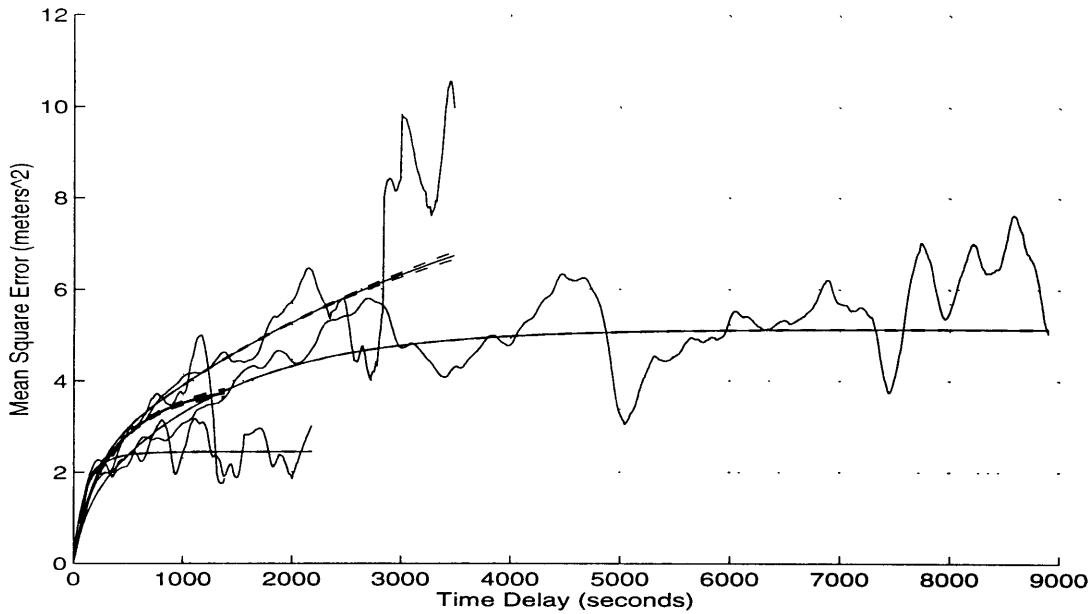


**Figure 4.22 Markov Fit, All Cases**

### 4.1.5 Residual Errors

All the residual errors shown have had sinusoidal characteristics. They are now examined more closely. Figure 4.23 plots the model residuals for all three of the previ-

ous cases. Not only are the sinusoidal characteristics evident in each, but the same frequency and phase is present.

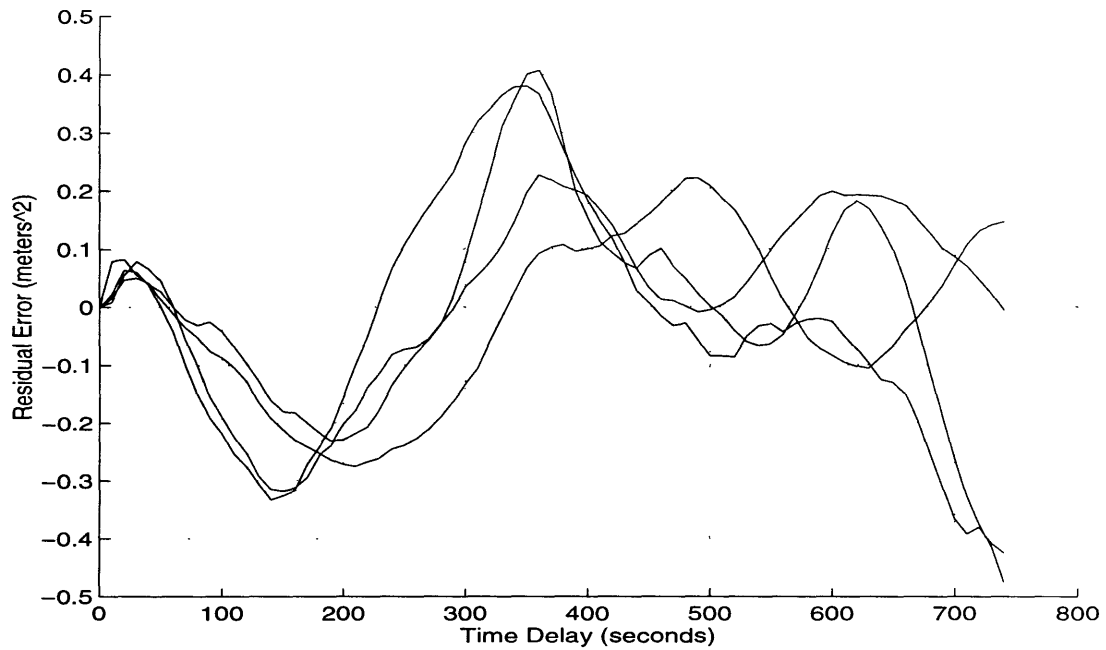
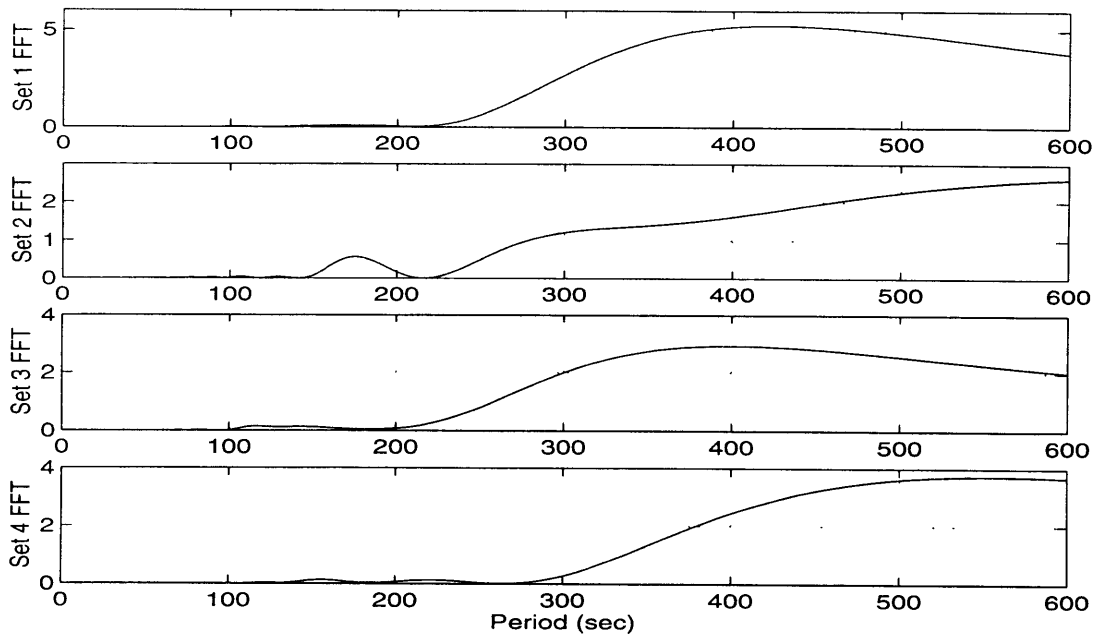


**Figure 4.23 Residual Errors, All Cases**

Figure 4.24 shows the FFT for each of the model residuals. The periods of the oscillations are very similar for all four cases. A primary period of about 400 seconds



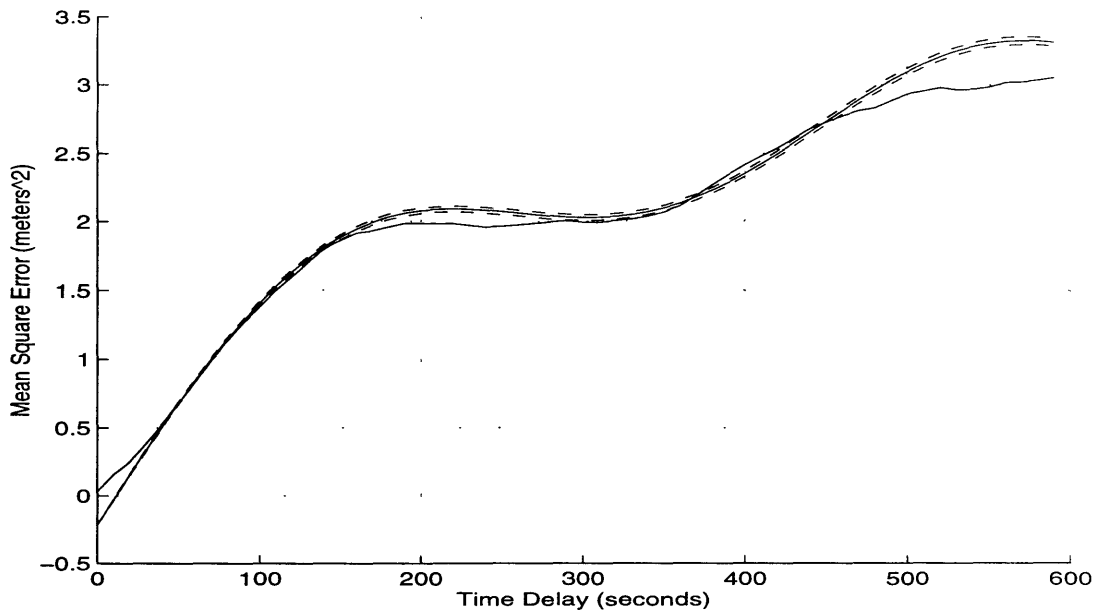
is apparent. The next step is to see if the Markov model fits the data better if appropriate sinusoidal terms are added.



**Figure 4.24 FFT for Residuals**

A sinusoidal term using the period identified was added to the Markov model to attempt a better fit. The new fit is shown in Figure 4.25. This fit is much better than the Markov process alone. The model for the residual used is given in Equation (4.7). The short period of this oscillation once again points to multipath. Some particular, strong reflected signal common to all cases is a possible explanation

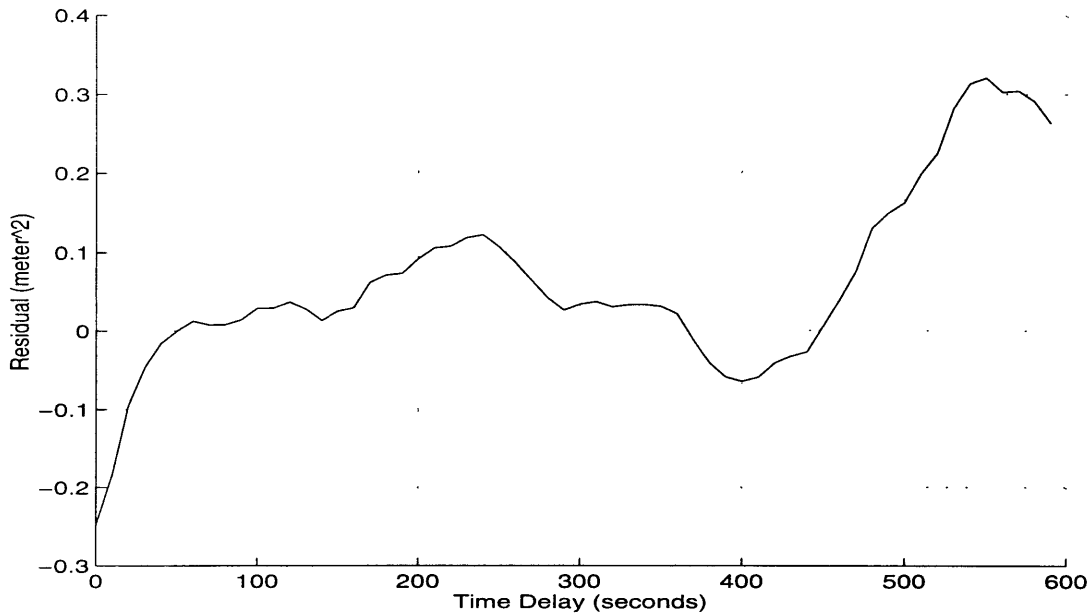
$$\text{Res} = 0.35 \sin \left[ 2\pi \left( \frac{1}{400} \right) (t + 150) \right] \quad (4.7)$$



**Figure 4.25 New Model Fit to Data**

Figure 4.26 shows the residual for the new model. Note that the amplitude of the residual has been reduced to about a fourth of its former level. Note that sinusoidal characteristics can still be observed in the data. Further reduction using these periods

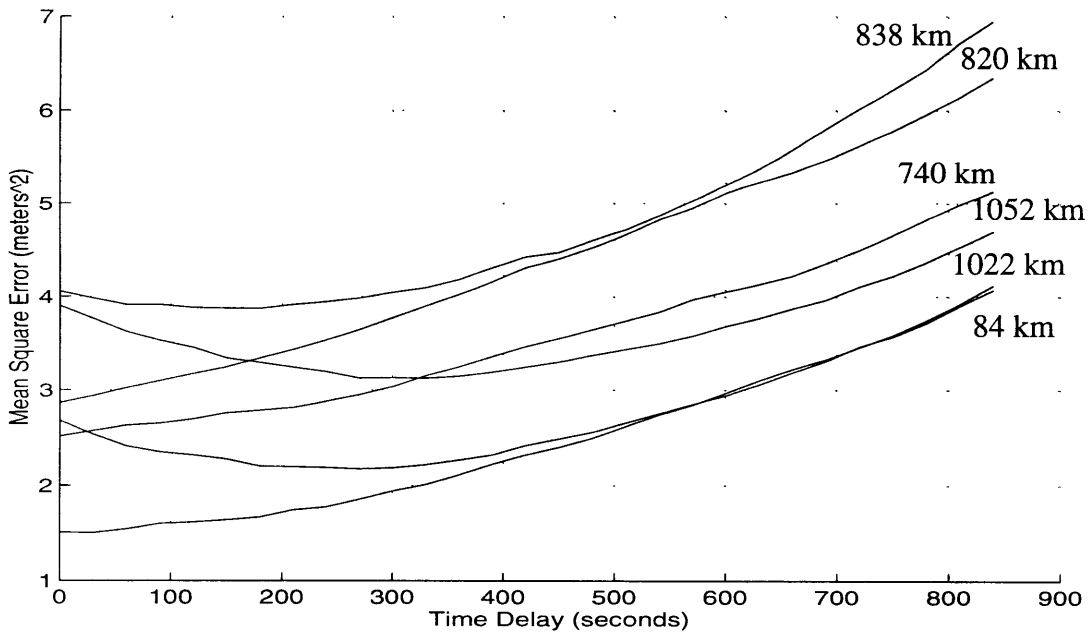
is possible. The primary periods in these residuals match those found in the time delay data in Chapter 3.



**Figure 4.26 Residual for New Markov/Sinusoid Fit**

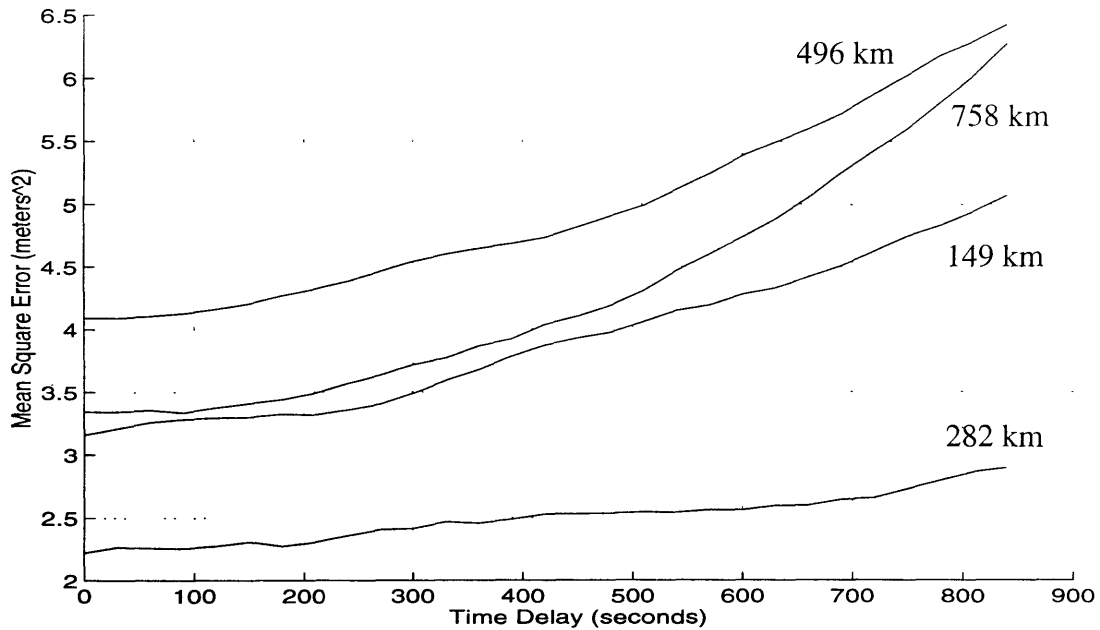
## 4.2 East and West Coast Experiment Results

Figure 4.27 shows the results for the East Coast baselines.



**Figure 4.27 East Coast Baseline Results**

Figure 4.28 shows the results from the West Coast data.



**Figure 4.28 West Coast Baseline Results**

The errors shown in Figure 4.27 and Figure 4.28 include the effects of multipath. An estimate of errors due to multipath was obtained using the same process that was used for the zero baseline data. That is, time shift differences were made, and a dual Markov model was fit to these differences. The shorter time constant was consistent with multipath effects. The variances were somewhat smaller than seen on the rooftop. Variances for each pair were obtained by combining the appropriate values. These variances are shown in Table 4.3. They were subtracted from the errors before proceeding to find a combined time delay/distance model.

**Table 4.3 Multipath Variances for Each Baseline**

Separation (km)	Locations	$\sigma_{\text{multi}}^2$ (meters <sup>2</sup> )
84	Draper/Portsmouth	0.22
149	Long Beach/San Diego	0.92
282	Fallon/Stockton	0.67
496	Fallon/Fort Irwin	0.90

**Table 4.3 Multipath Variances for Each Baseline**

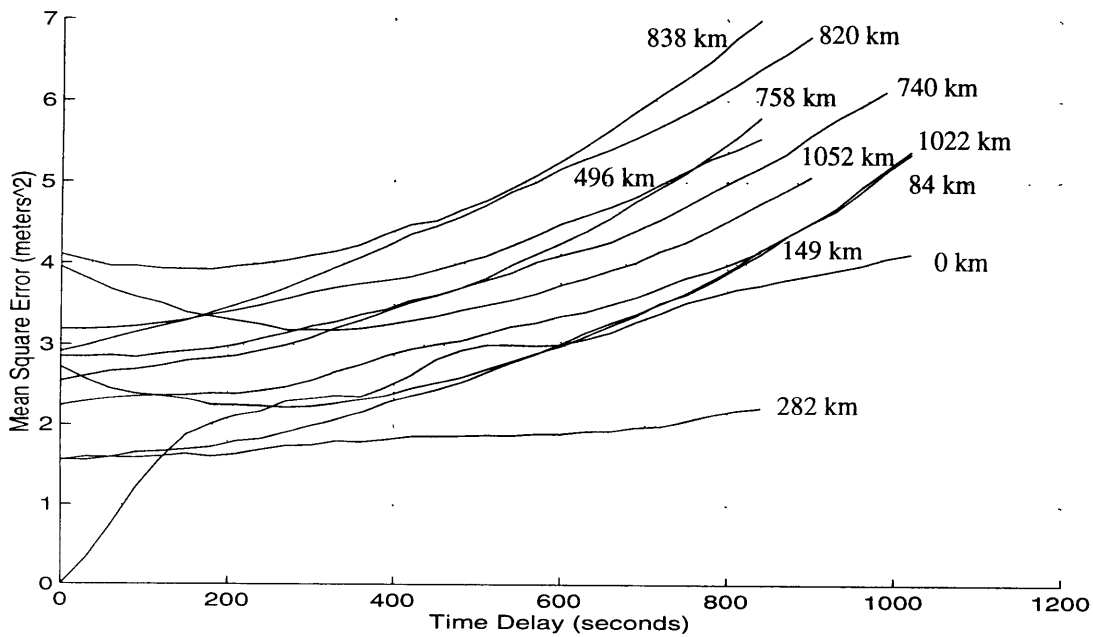
Separation (km)	Locations	$\sigma_{\text{multi}}^2$ (meters <sup>2</sup> )
740	Langley/Draper	0.18
756	Fallon/San Diego	0.49
820	Langley/Portsmouth	0.10

### 4.3 Combined Model

The results have been presented for each of the three data sources: zero baseline, East Coast, and West Coast. Now the results from the navigation solution errors will be combined to create composite results. The 24-hour data for the zero baseline case will be used since it has a longer time base.

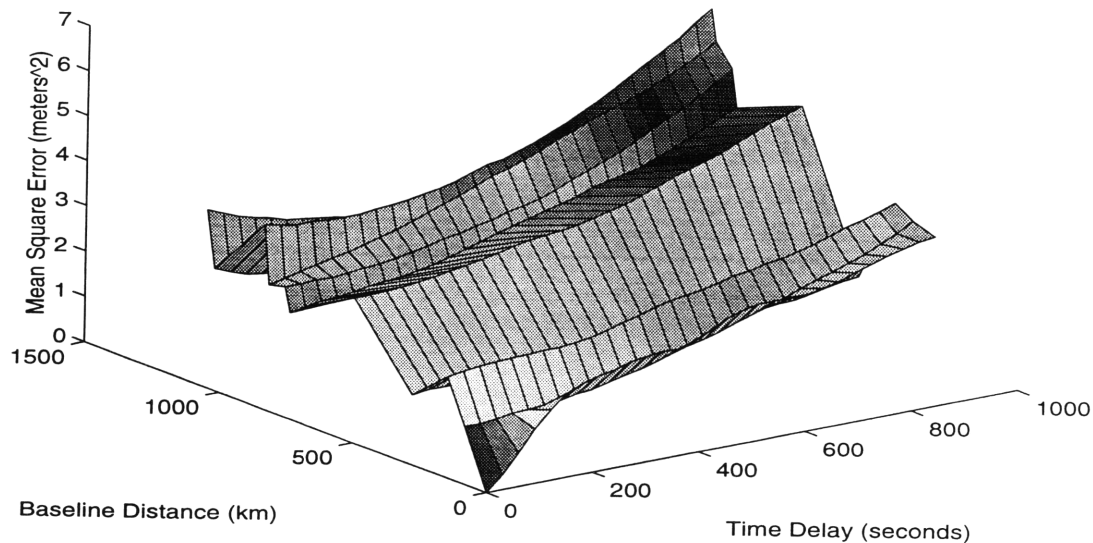
#### 4.3.1 Results From All Sets

Figure 4.29 plots all baseline errors together.



**Figure 4.29 Navigation Solution Errors, All Data Sets**

Figure 4.30 plots the same information in 3-D format for a more visual interpretation.



**Figure 4.30 3-D Error Plot, All Data Sets**

Figure 4.31 plots a cross section of the 3-D plot at zero time delay. This cross section will be used to fit the Markov process for the distance correlation. The last three points are from the East Coast baselines with a C/A-code receiver at one end (Willow Run). The Draper data collection personnel indicated a lower confidence in the output from these receivers. In addition, the selective availability errors had to be removed by Aerospace in post processing. By policy, these errors were not totally removed from the data, and some noise still remains. Given these facts, a strong case can be made for

the removal of the C/A-code runs from the data sets. This would leave only P-code data leading to a higher confidence in the results.

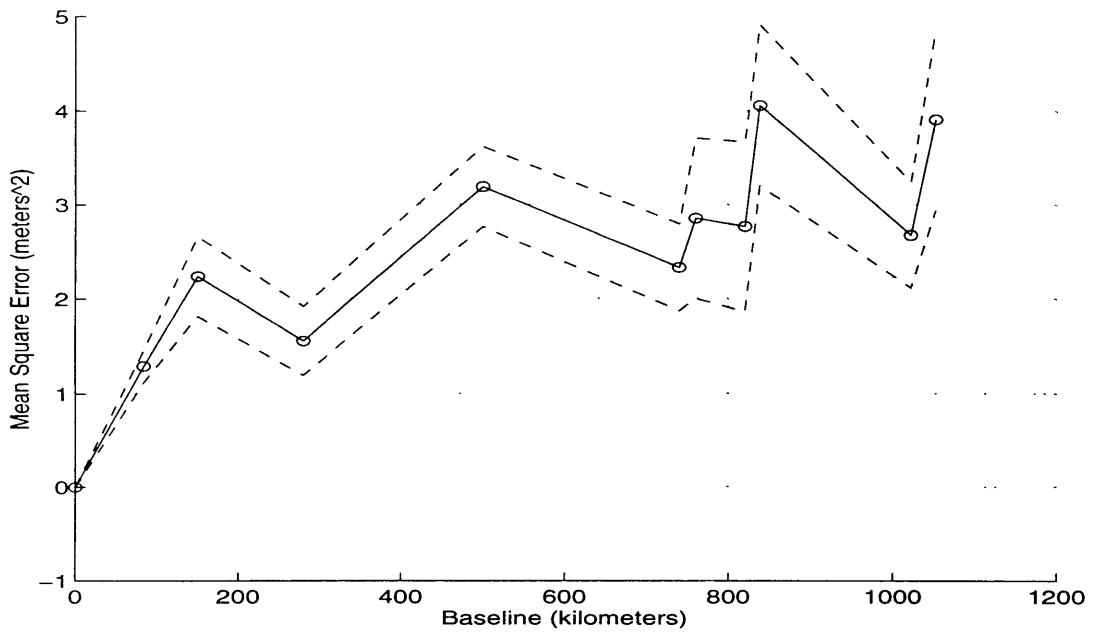


**Figure 4.31 Zero Time Delay Results, All Data Sets**

### 4.3.2 Results From High Confidence Sets

To create a set of high confidence data, the three C/A-code sets at 838, 1022 and 1052 km were removed. The resulting time delay errors are shown in Figure 4.32.

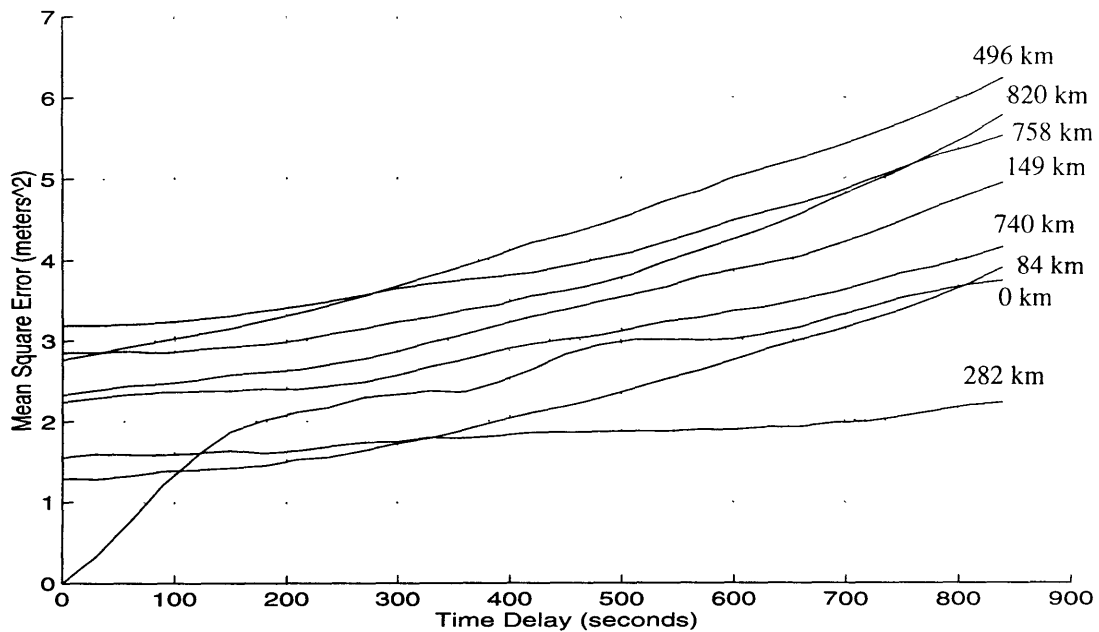
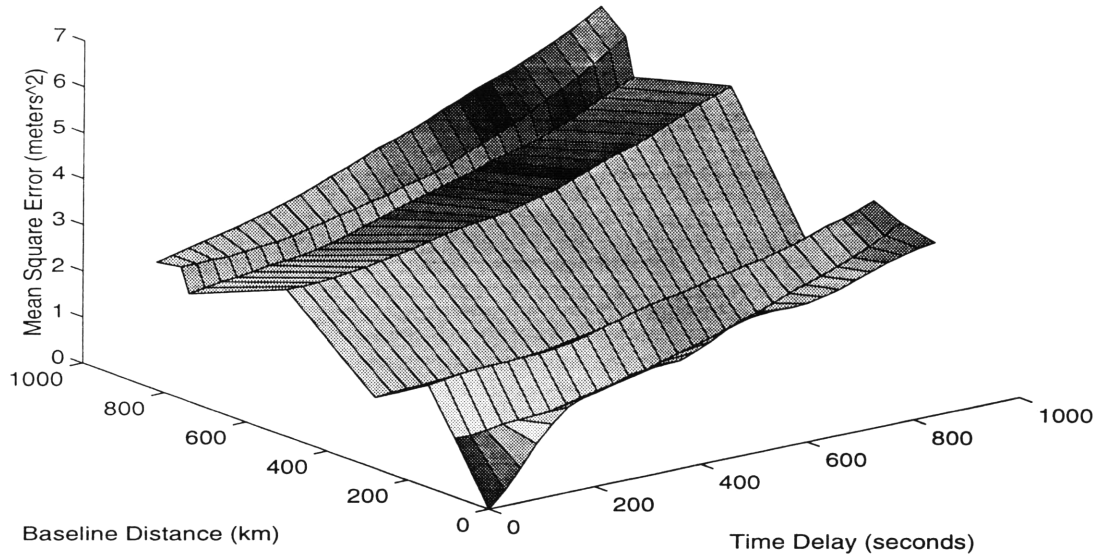


Figure 4.32 Time Delay Errors, High Confidence Sets

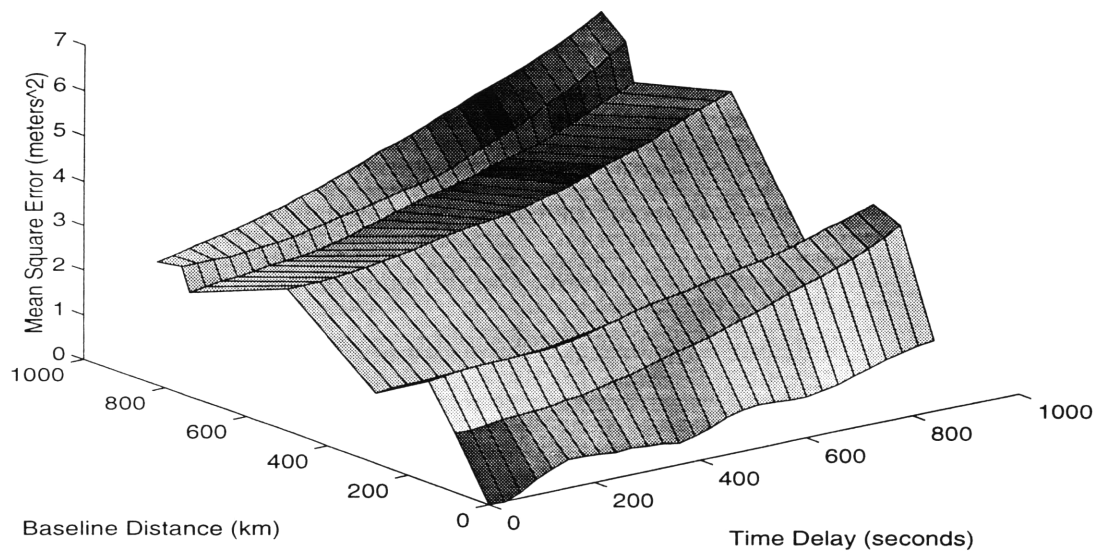


Figure 4.33 shows the 3-D plot for the high confidence data sets. Note that this surface is smoother than the one including the C/A-code results.



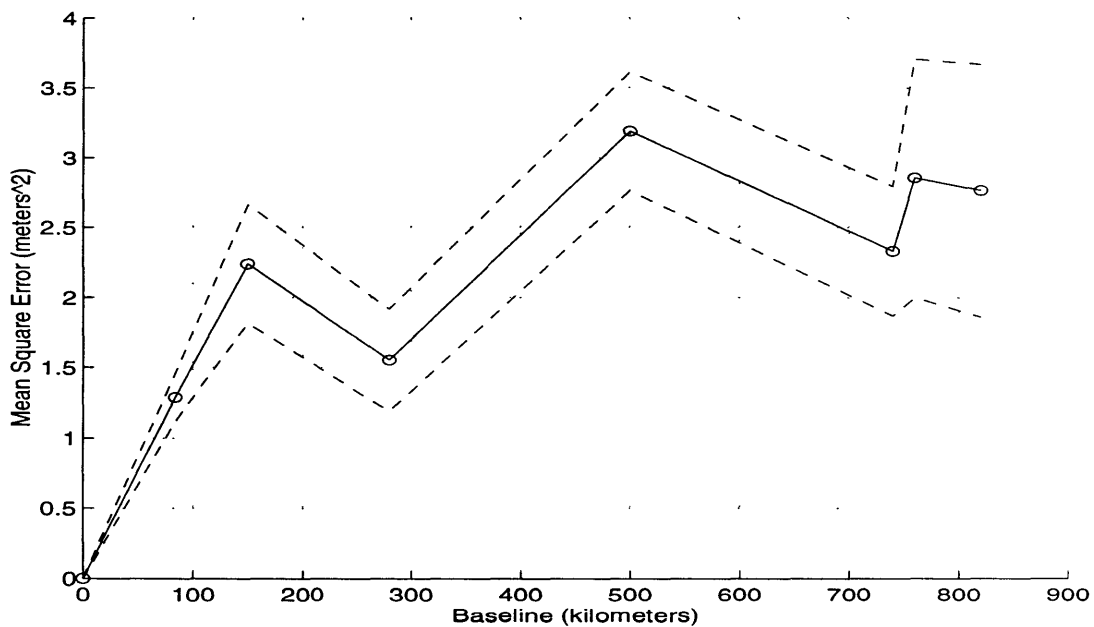
**Figure 4.33 3-D Error Plot, High Confidence Sets**

Figure 4.34 shows the 3-D plot for the high confidence data sets with the multipath removed from the zero baseline data. This plot will be compared with the final model.



**Figure 4.34 3-D Error Plot, No Multipath**

Figure 4.35 plots the cross-sectional view of Figure 4.33 for the case with no time delay. This data is used as an input to the Marquardt method to fit the Markov model to the distance dimension. The 1-sigma error bounds provided to the Marquardt method are also shown in the graph. The circles show the actual data points available for the Marquardt fit. Note that even with several baselines of collected data, there are still very few points in the distance dimension compared with the number of points in the time delay dimension.



**Figure 4.35 Zero Time Delay Results, High Confidence Sets**

Figure 4.36 shows the Markov fit for the distance dimension. The bias is zero because the 24-hour data was used at 0 km, and only one receiver was available for this data. Equation (4.8) shows the model that was used in the Marquardt fitting routine for the distance dimension.

$$\text{Model} = \sigma_1^2 \left( 1 - e^{-\frac{x}{\lambda_c}} \right) \tag{4.8}$$

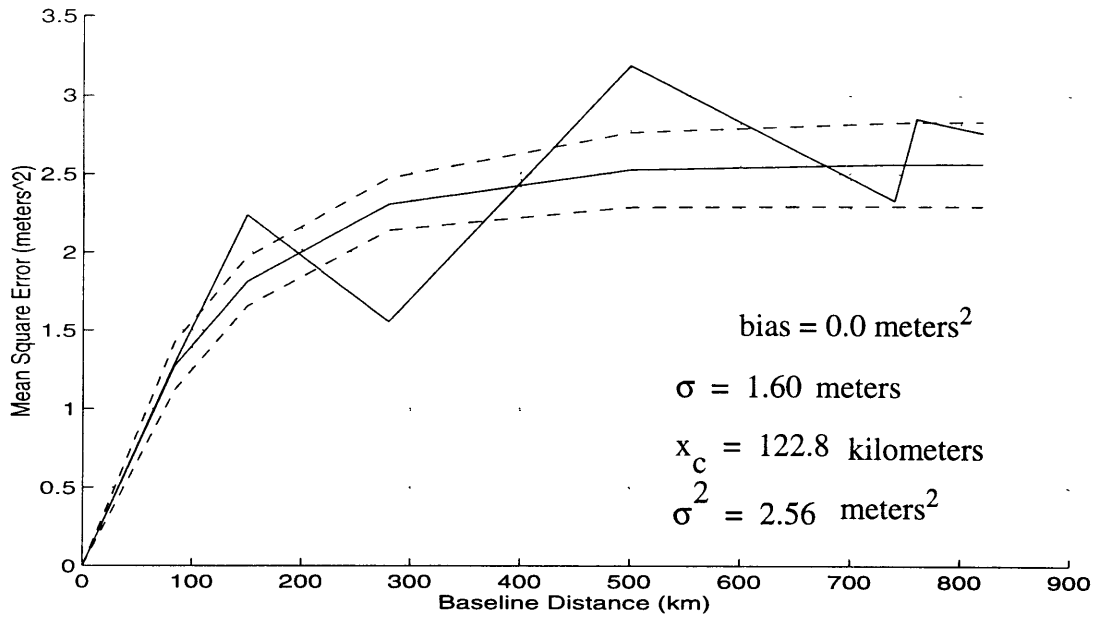


**Figure 4.36 Markov Process Fit, Distance Dimension**

Figure 4.37 plots the residual for the distance dimension Markov fit. There is a slight sinusoidal characteristic to this plot, but not enough data points are available to merit trying to correct the model.

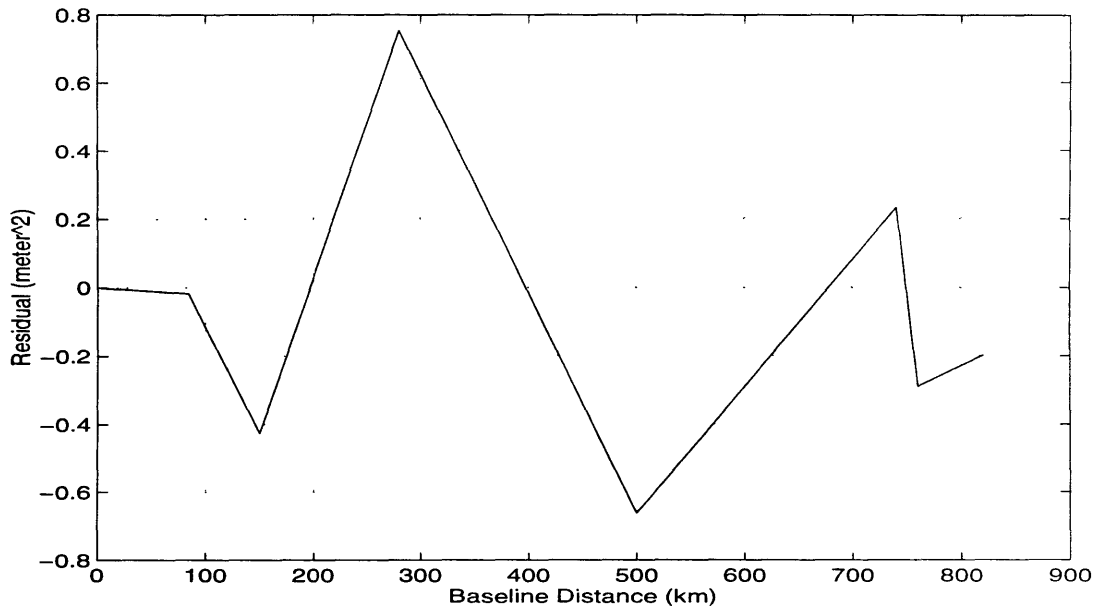


**Figure 4.37 Residual for Markov Fit, Distance Dimension**

Figure 4.38 shows the final resulting DGPS model obtained by combining the Markov fit to the time delay and baseline distance dimensions. Since the same underlying phenomena cause the distance and time decorrelation, the variance of the process is common. The value of 3.73 meters<sup>2</sup> is the weighted average of the values found for the time and distance models. Note that the raw data has a significant spread and this model will not encompass every case. Rather it is meant to provide an average error model that represents the typical behavior of the DGPS operation. The formula for the DGPS model is given by Equation (4.9). This plot can be compared with Figure 4.34. Note that these results have been normalized by the DOP values. To determine the errors obtained in the navigation solution, the model must be multiplied by the appropriate DOP values for the given satellite geometry.

$$MS = 3.73 \left( 1 - e^{-\frac{t}{3847.1} - \frac{x}{122.8}} \right) \quad (4.9)$$

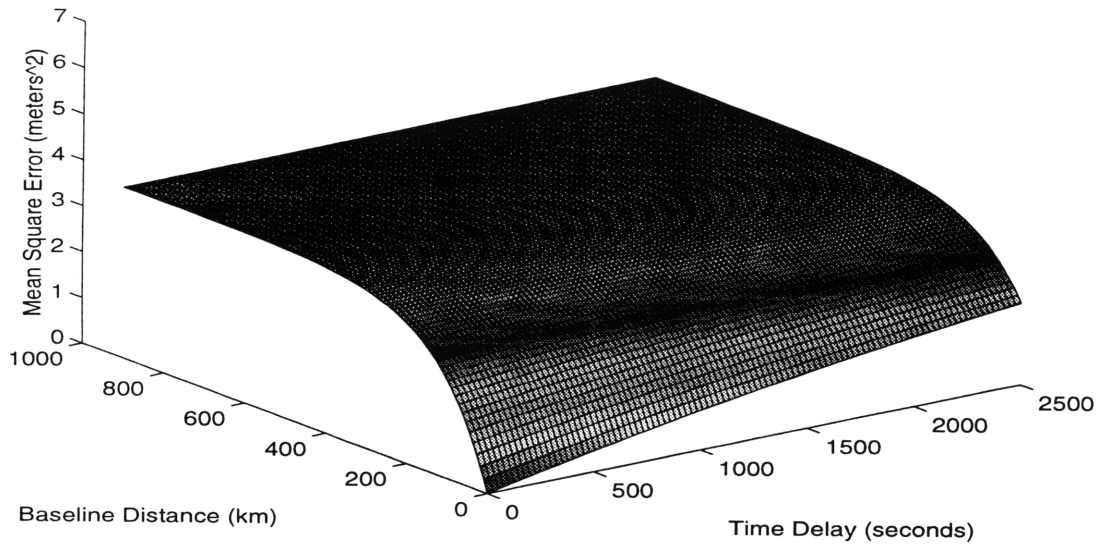


**Figure 4.38 DGPS Error Model**

The data used to determine the time constant,  $\tau$ , comes exclusively from the “roof-top” experiments. This is because the data from the East and West Coast experiments was not of sufficient duration to contribute much to the determination of  $\tau$ .



## Chapter 5

### Conclusions and Suggestions for Future Work

This thesis analyzed GPS data collected by Draper Laboratory to determine DGPS error characteristics. It was found that a first order Markov process could be used as an appropriate model for the errors in differential GPS. Since the errors are correlated in both time and distance, the Markov model has a process variance, a time correlation constant, and a distance correlation constant. Analysis of both navigation solution errors and pseudorange bias errors provided a wide range of data sets for processing. The Marquardt non-linear curve fitting routine was used to obtain the parameters for the Markov model for each set of data.

#### 5.1 Conclusions

The resulting DGPS model is given in Equation (5.1).

$$MS = 3.73 \left( 1 - e^{-\frac{t}{3847.1} - \frac{x}{122.8}} \right) \text{ meters}^2 \quad (5.1)$$

where MS is the mean square error in the pseudorange biases.

This model is fairly representative of average navigation solution errors. It should be noted that there are significant deviations from nominal performance. (Refer to Figure 4.8 for example.) The analyst might wish to choose a larger value for the variance to describe “worst case” performance. The rationale for using a Markov fit is that many physical processes tend to exhibit Markov-like behavior and that it is a convenient model for linearized analysis.

The error model is consistent with the differential GPS error budget given in Chapter 1. The DGPS budget had a MS error of 1.59 meters<sup>2</sup>, (1.26<sup>2</sup>). The Markov model determined herein has a MS error of 3.73 meters<sup>2</sup>. The variance at 92.6 km separation and zero time delay is about 1.98 meters<sup>2</sup>. Fifty nautical miles (92.6 kilometers) is the distance assumed in the referenced error budget. Multipath effects could easily account for the difference. The referenced budget is only the specification for the system and not necessarily indicative of actual performance.

The raw data has a significant spread to it depending on the time of day, geometry, multipath, weather conditions, and possibly other factors. This model does not encompass every facet of the error sources. In particular we have seen the importance of multipath error modeling. An attempt was also made to correlate the magnitude of the time delay errors to the time of day. Few data points were available, but the results indicate the lowest values occur during the afternoon and early evening. This would mean that the output from the two receivers is more highly correlated at these times.

The model was developed by analyzing the errors in the navigation solution output of the GPS receivers. The individual pseudorange errors that contribute to the position error were also examined. A technique was developed to attribute changes in all pseudorange errors at satellite switch to changes in the user clock bias error estimate. This indeed caused the pseudorange error for each satellite to be continuous and not experience jumps when a satellite switch occurred. The results from this analysis were consistent with those obtained from the navigation solution analysis for the zero baseline data. While this is encouraging, and lends more credibility to the determination of the time constant, the lack of a measure for true GPS time means the value for pseudorange error determined in this manner will be consistently low.



The cross-correlation technique was ineffective at determining the Markov fit parameters. This is due to the requirement for large continuous data sets for cross-correlation accuracy. DGPS data sets are limited to about one hour due to satellite switches. Alternatively, the Marquardt curve fitting routine was used to fit the time delay error to a Markov process. This routine also allowed fitting of two independent processes.

This thesis effort has revealed many interesting aspects of the GPS receiver operation including a close look at P-code data from two receivers attached to the same antenna. Of biggest importance may be the dramatic change in amplitude and frequency of oscillations in the navigation solution at each point where a satellite switch occurs. Given that multipath is the cause of such behavior, shielding or other countermeasures should be investigated on future experiments or in operational scenarios.

## **5.2 Future Work**

As just mentioned, multipath should be treated more carefully in future experiments. It should be eliminated in order to examine other error sources and should be introduced in a controlled fashion if desired.

Internet GPS data may be able to provide longer sets of data where the restriction of common satellites in each set is no longer a requirement. In order to obtain this, the best sites with accurately surveyed positions and hydrogen maser clocks would provide the best opportunity for such data. This data would provide a check against the work done in this thesis and provide more insight into the correlation constants obtained. The best Internet address to use for these sources is [toba.ucsd.edu](http://toba.ucsd.edu). It is not clear, however, how the errors such as selective availability can be completely separated from the other physical errors of interest. The Internet receivers are not

encrypted, so SA will be present. Since the position is known very accurately, the errors in the navigation solution will be known very accurately, but the contribution from each error source can only be estimated.

Even if true GPS time is unavailable at the receiver, a comparison of Time Dilution of Precision (TDOP) values with the PDOP values could be utilized to obtain a statistical estimate of the receiver clock errors. This would allow inclusion of these errors into the estimate of the pseudorange errors combined with the adjustment of clock bias devised herein. This would allow longer data sets to be analyzed. Short segments of data were one of the primary limitations for this thesis effort.

# Appendix A

## Marquardt Method

The Marquardt method or Levenberg-Marquardt method provides a way to perform non-linear curve fitting for data. The process defines a chi-squared ( $\chi^2$ ) merit function and determines best-fit parameters by minimizing the merit function. For the nonlinear case, the minimization is performed iteratively. The procedure is repeated until  $\chi^2$  effectively stops decreasing. Numerical Recipes [22] explains the Marquardt method in detail. The main points will be discussed here.

The model to be fitted is

$$y = y(x_i; \bar{a}) \quad (\text{A.2})$$

where  $\bar{a}$  is the vector of parameters in the model that the Marquardt method must find. In this case,  $\bar{a} = [\sigma \ \tau]$  and  $y = \sigma^2 \left( 1 - e^{-\frac{x_i}{\tau}} \right)$ . The  $\chi^2$  merit function is

$$\chi^2(\bar{a}) = \sum_{i=1}^N \left[ \frac{y_i - y(x_i; \bar{a})}{\sigma_i} \right]^2 \quad (\text{A.3})$$

The goal of the Marquardt method is to find  $\bar{a}_{\min}$  that minimizes  $\chi^2$ . An initial guess called  $\bar{a}_{\text{cur}}$  is required to get things started. If the guess for  $\bar{a}$  is fairly good, the second derivative matrix (Hessian matrix) of the  $\chi^2$  function is used to jump immediately to the  $\bar{a}_{\min}$  for that guess using

$$\bar{a}_{\min} = \bar{a}_{\text{cur}} + D^{-1} \cdot [-\nabla \chi^2(\bar{a}_{\text{cur}})] \quad (\text{A.4})$$

where D is the Hessian matrix.

However, if the guess is poor, the inverse-Hessian method cannot be used. In this case, the steepest descent method is used to take a step down the gradient

$$a_{\text{next}} = a_{\text{cur}} - \text{constant} \times \nabla \chi^2(a_{\text{cur}}) \quad (\text{A.5})$$

where the constant is small enough not to exhaust the downhill direction.

The gradient of  $\chi^2$  with respect to the parameters  $\bar{a}$ , which will be zero at the  $\chi^2$  minimum, has components

$$\frac{\partial \chi^2}{\partial a_k} = -2 \sum_{i=1}^N \frac{[y_i - y(x_i; \bar{a})]}{\sigma_i^2} \frac{\partial}{\partial a_k} y(x_i; \bar{a}) \quad k = 1, 2, \dots, M \quad (\text{A.6})$$

Taking an additional partial derivative gives

$$\frac{\partial^2 \chi^2}{\partial a_k \partial a_l} = 2 \sum_{i=1}^N \frac{1}{\sigma_i^2} \left[ \frac{\partial}{\partial a_k} y(x_i; \bar{a}) \frac{\partial}{\partial a_l} y(x_i; \bar{a}) - [y_i - y(x_i; \bar{a})] \frac{\partial^2}{\partial a_k \partial a_l} y(x_i; \bar{a}) \right] \quad (\text{A.7})$$

The following terms are defined

$$\beta_k \equiv -\frac{1}{2} \frac{\partial \chi^2}{\partial a_k} \quad \alpha_{kl} \equiv \frac{1}{2} \frac{\partial^2 \chi^2}{\partial a_k \partial a_l} \quad (\text{A.8})$$

Now  $[\alpha] = \frac{1}{2} D$  in Equation (A.4) which can be rewritten

$$\sum_{i=1}^M \alpha_{ki} \delta a_i = \beta_k \quad (\text{A.9})$$

This set of linear equations can be solved for the increments  $\delta a_i$  that are added to the current approximation to get the next approximation.

The steepest descent formula translates to

$$\delta a_i = \text{constant} \times \beta_i \quad (\text{A.10})$$

The Marquardt method allows the smooth variation between the steepest descent method and the inverse-Hessian method as the approximation goes from poor to good. The two methods are combined into one equation

$$\sum_{i=1}^M \alpha'_{ki} \delta a_i = \beta_k \quad (\text{A.11})$$

where  $\alpha'$  is given by

$$\begin{aligned} \alpha'_{jj} &\equiv \alpha_{jj} (1 + \lambda) \\ \alpha'_{jk} &\equiv \alpha_{jk} \quad (j \neq k) \end{aligned} \quad (\text{A.12})$$

and  $\lambda$  is referred to by the author as a non-dimensional fudge factor. If  $\lambda$  is large, the approximation is poor, and the steepest descent method is used. If  $\lambda$  is near zero, the approximation is good, and the inverse-Hessian method is used.

The Marquardt recipe consists of the following:

- Compute  $\chi^2(\bar{a})$
- Pick a modest value for  $\lambda$ , say  $\lambda = 0.001$ .
- (1) Solve Equation (A.11) for  $\delta\bar{a}$  and evaluate  $\chi^2(\bar{a} + \delta\bar{a})$
- If  $\chi^2(\bar{a} + \delta\bar{a}) \geq \chi^2(\bar{a})$ , *increase*  $\lambda$  by a factor of 10 and return to (1)
- If  $\chi^2(\bar{a} + \delta\bar{a}) < \chi^2(\bar{a})$ , *decrease*  $\lambda$  by a factor of 10, update the trial solution  $\bar{a} \leftarrow \bar{a} + \delta\bar{a}$ , and return to (1).

Once the acceptable minimum is found (change in  $\chi^2$  of less than 0.1),  $\lambda$  is set to zero and the covariance is found

$$[C] \equiv [\alpha]^{-1} \quad (\text{A.13})$$

The partial derivatives of the model with respect to the individual parameters in  $\bar{a}$  are used by the Marquardt method. For the Markov exponential fit, the partials are

$$\frac{\partial y}{\partial \sigma} = 2\sigma \left( 1 - e^{-\frac{x}{\tau}} \right) \quad (\text{A.14})$$

$$\frac{\partial y}{\partial \tau} = \frac{-\sigma^2 x e^{-\frac{x}{\tau}}}{\tau^2} \quad (\text{A.15})$$

## Appendix B

### Autocorrelation Limits

The limits on the experimental autocorrelation function were found in [7]. The initial assumption proven in [3] is that the variance of an experimentally determined autocorrelation function satisfies the inequality

$$\text{Var}V_x(\tau) \leq \frac{4}{T} \int_0^{\infty} R_x^2(\tau) d\tau \quad (\text{B.1})$$

where  $T$  = time length of the experimental record

$R_x(\tau)$  = autocorrelation function of the Gaussian process under consideration

$V_x(\tau)$  = time average of  $X_T(t)X_T(t+\tau)$  where  $X_T(t)$  is the finite-length sample of  $X(t)$  (that is,  $V_x(\tau)$  is the experimentally determined autocorrelation function based on a finite record length)

The experimental autocorrelation is formed by

$$V_x(\tau) = \frac{1}{T-\tau} \int_0^{(T-\tau)} X_T(t) X_T(t+\tau) dt \quad (\text{B.2})$$

It is noted here that the Matlab function `xcorr` does not divide by  $\frac{1}{T-\tau}$ , so the user must be careful when working with that function. Dividing properly will result in Equation (B.2).

$V_x(\tau)$  can be shown to be an unbiased estimator of  $R_x(\tau)$  [7]. Assuming that the process  $X(t)$  is a Gauss-Markov process, then the autocorrelation function is

$$R_x(\tau) = \sigma^2 e^{-\beta|\tau|} \quad (\text{B.3})$$

Note that  $\beta = \frac{1}{\tau}$ . This autocorrelation can be substituted in Equation (B.1) to give

$$\text{Var}[V_x(\tau)] \leq \frac{2\sigma^4}{\beta T} \quad (\text{B.4})$$

which is the limit that is used for the accuracy on an experimental autocorrelation function in Chapter 3.



## References

- [1] Axelrad, P., Chesley, B., "Performance Testing of a GPS Based Attitude Determination System", AIAA-93-3787-CP.
- [2] Beck, J. V., Arnold, K. J., *Parameter Estimation in Engineering and Science*, John Wiley & Sons, New York, NY, 1977.
- [3] Bendat, J. S., Piersol, A. G., *Random Data: Analysis and Measurement Procedures*, Wiley-Interscience, New York, NY, 1971.
- [4] Blackwell, E. G., "Overview of Differential GPS Methods", *Global Positioning System Navigation, The Institute of Navigation*, 1993
- [5] Brown, A., "Extended Differential GPS", *Navigation: Journal of The Institute of Navigation*, Vol. 36, No. 3, Fall 1989.
- [6] Brown, D., Personal communication with author, The Charles Stark Draper Laboratory, Inc., Cambridge, MA, November 1994.
- [7] Brown, R. and Hwang, P., *Introduction to Random Signals and Applied Kalman Filtering*, John Wiley & Sons, Inc., New York, NY, 1983.
- [8] Chi, T., et al., "Differential GPS Covariance Error Model", Draper Laboratory Memorandum ESB-92-200, April 15, 1992.
- [9] Fikes, M., "Relative Targeting with Differential GPS and Associated Error Mechanisms", Draper Laboratory Memorandum ESB-93-535, July 28, 1993.
- [10] Fink, B., Personal communication with author, The Charles Stark Draper Laboratory, Inc., Cambridge, MA, November 1994.
- [11] Fisz, M., *Probability Theory and Mathematical Statistics*, John Wiley & Sons, Inc., New York, NY, 1963.
- [12] Gelb, A., *Applied Optimal Estimation*, The M.I.T. Press, Cambridge, MA, 1974.
- [13] Glushik, J., "Data Analysis and Accuracy Performance of Multisite Differential GPS", Master's Thesis, Massachusetts Institute of Technology, May 6, 1994.
- [14] Harkleroad, G., et al., "Estimation of Error Correlation Distance for Differential GPS Operation", *IEEE Position Location and Navigation Symposium Record*, 1990.
- [15] "High Dynamic Instrumentation Set (HDIS) Specification", YISP-83-14, United States Air Force (AD/YI), Eglin AFB, Florida, July 1984.
- [16] Jurgens, R. D., "Realtime GPS Azimuth Determining System", *Proceedings of ION National Technical Meeting*, San Diego, CA, January 23-25, 1990.
- [17] Kalafus, R., et al., "Differential Operation of NAVSTAR GPS", *Global Positioning System, vol. II, The Institute of Navigation*, 1983.
- [18] Kalafus, R., et al., "Special Committee 104 Recommendations for Differential GPS Service", *Global Positioning System Navigation, The Institute of Navigation*, 1986.
- [19] Lapucha, D., Huff, M., "Multisite Real-Time DGPS System Using Satellite Data

- Link: Operational Results”, *Navigation: Journal of The Institute of Navigation*, Vol. 40, No. 3, Fall 1993.
- [20] Milliken, R., Zoller, C., “Principle of Operation of NAVSTAR and System Characteristics”, *Navigation: Journal of The Institute of Navigation*, Vol. 25, No. 2, Summer 1978.
- [21] Mullen F., Personal communication with author, The Charles Stark Draper Laboratory, Inc., Cambridge, MA, November 1994.
- [22] Press. H., et al., *Numerical Recipes*, Cambridge University Press, Cambridge, MA, 1986.
- [23] Rankin, J., “GPS and Differential GPS: An Error Model for Sensor Simulation”, *IEEE Position Location and Navigation Symposium Record*, 1994.
- [24] Rocken, C., Meertens, C., “Monitoring Selective Availability Dither Frequencies and Their Effect on GPS Data”, *Bulletin Geodesique*, Spring, 1991.
- [25] Sennott, J. W., Pietraszewski, D., “Experimental Measurement and Characterization of Ionospheric and Multipath Errors in Differential GPS”, *Navigation: Journal of the Institute of Navigation*, vol. 34, no. 2, Summer 1987.
- [26] Shepperd, S., “Deterministic GPS Solution in Closed-Form”, Draper Laboratory Memorandum ESB-94-319, June 8, 1994.

7-11-94